Glacial Ice Actions

Executive Summary of NORD ST20 2019/313 and NORD ST19

Petroleumstilsynet

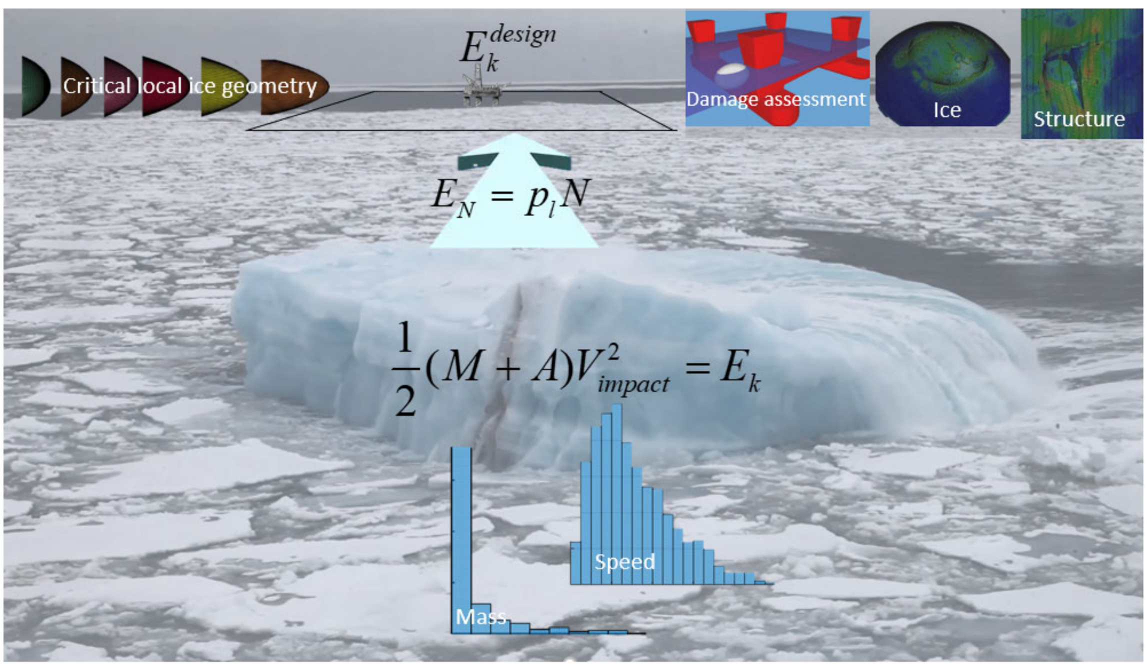

Report NO: ArcISo_2019_Ptil03

By ArcISo AS

Date: 16/01/2020

<table>
<tr><td colspan="2">ArcISo
Arctic Integrated Solutions
Address: NO-7034 Trondheim, Norway
Location: Gløshaugen Høgskolerigen 7A
Managing director: Raed Lubbad (+47 735 94 583)
Email: raed.lubbad@ntnu.no
Enterprise NO: 917100454
Website: https://arciso.com</td><td colspan="2">ArcISo AS
AUTHOR(S)
Wenjun Lu, Zhaolong Yu, Raed Lubbad, Jørgen Amdahl, Sveinung Løset, Ekaterina Kim</td></tr>
<tr><td colspan="2">TITLE
Glacial Ice Actions: Executive summary of NORD ST20_2019/313 and NORD ST19</td><td colspan="2">CLIENT(S)
Petroleumstilsynet (Petroleum Safety Authority Norway)</td></tr>
<tr><td>CLASS. THIS PAGE
Open</td><td>PROJECT MANAGER
Wenjun Lu</td><td>PROJECT NO
ST20_2019/313_Extension</td><td>NO OF PAGES
55</td></tr>
<tr><td colspan="2">APPROVED BY
Raed Lubbad (ArcISo Managing Director)</td><td colspan="2" rowspan="2">CHECKED BY
Jørgen Amdahl
Sveinung Løset
Raed Lubbad</td></tr>
<tr><td>REPORT NO
ArcISo_2019_Ptil03</td><td>DATE
16.01.2020</td></tr>
</table>

ABSTRACT

This report is an executive summary of the two preceding projects, i.e., NORD ST20 2019/313 and NORD ST19. The overarching processes from modelling the glacial ice conditions, to calculating the glacial ice action and to assessing the structural damage were summarised in forms of:

- existing knowledge,
- modelling approaches,
- the design philosophy,
- and involved major physical process.

Efforts were made to construct the framework to allocate the knowledge accumulated in previous projects within and in line with existing standards. In addition, detailed recommendations in forms of suggested practices and formulations are supplied in the annexes.

KEY WORDS: Glacial Ice Actions, Glacial Ice Conditions, NORSOK, ISO19906, Damage assessment, Impact, Ice, Nonlinear FEM

Glacial Ice Actions
Executive summary of NORD ST20 2019/313 and NORD ST19

Contents

1 Background

This report is written by ArcISo AS for the Petroleum Safety Authority (PSA) as an executive summary of the two projects, i.e., NORD ST20 2019/313 (Lu et al., 2019) and NORD ST19 (Lu et al., 2018). To achieve the best application of the learnings, the larger context of existing standards is taken into account while formulating this executive summary report.

2 Terminology

2.1 Terms and definitions

2.1.1 Glacial ice features

Glacial ice features are all types of glacial or shelf ice features that have broken (calved) away from its source

2.1.2 Icebergs

Same definition as in ISO19906 (2019) is adopted. *Iceberg* is defined as glacial or shelf ice with maximum sail height greater than 5 m that has broken (calved) away from its source.

2.1.3 Glacial ice / Ice

In this report, the terms 'glacial ice' and 'ice' are used interchangeably. The term 'ice' in the current report's context refers specifically to glacial ice features. Derived terminologies ice conditions, ice actions, ice deformation, ice impacts correspond to glacial ice conditions, glacial ice actions, glacial ice deformation, and glacial ice features' impact respectively.

2.1.4 Global and local ice drift model

The global and local model both deal with the drift of glacial ice features under the action of wind, wave and current, and under both thermal and mechanical erosions. These two modelling processes differ mainly in the modelling scale, resolutions and the main results they are producing. The global model considers, for example, the entire Barents Sea and calculates the number (and global geometries) of glacial ice features entering a local domain (e.g., 100 km by 100 km) to be modelled by the local model. The local model additionally considers the structure size within the local domain and produce the local probability of collision. A joint result of these two models is the encounter frequency of a given structure with glacial ice features.

2.1.5 Ice crushing failure

Ice crushing failure is ice under compressive loading is broken into a granular material containing very small ice particles

2.1.6 Ice deformation

Ice deformation is used to characterise ice deformation and fragmentation processes during ice impact with an installation. It is measured in terms of the distance between the undeformed contact point between the structure and the ice until the largest ice crushing depth along the impact direction.

2.1.7 Kinetic energy

The *kinetic energy* of a glacial ice feature relative to an installation. The kinetic energy is calculated from the mass and added mass of the glacial ice feature and the relative velocity between the ice and the installation.

2.1.8 Impact energy

The *impact energy* is a portion of the kinetic energy that must be dissipated as deformation (strain energy) in the ice and the installation at impact. It is calculated based on momentum and energy conservation during the impact between the ice and the installation.

In agreement with ISO19906 (2019), the following definitions apply:

"shall" indicates a requirement; "*should*" indicates a recommendation; "*may*" is used to indicate that something is permitted; "*can*" is used to indicate that something is possible, for example, that an organisation or individual is able to do something.

2.2 Abbreviations

2.2.1 ULS Ultimate Limit State

2.2.2 ALS Accidental Limit State

2.2.3 ICEBASE

Sea Ice Investigations in the Barents Sea

2.2.4 P-A curve

Process pressure-area curve, where the pressure is an average pressure over the nominal projected contact area A

2.2.5 (NL)FEM

(Nonlinear) Finite Element Method

2.2.6 MBD

Multi-body dynamics

2.2.7 ALE

Arbitrary Lagrangian and Eulerian formulation in FEM

3 Glacial Ice Conditions

3.1 General

Glacial ice conditions shall be quantified (from measurements or numerical simulations) preceding any calculations of ice actions and any assessment of structural damage. This includes:

- Statistical distributions of the mass and main dimensions (length, width, height) of glacial ice features in the area of interest.
- Areal density of glacial ice features in the area of interest.
- Mechanical and physical properties of the glacial ice in the area.
- Probability of glacial ice intrusions into the area of interest.
- Statistical distributions of glacial ice features' mean drift velocity and the residence time of these features within the area of interest.
- The annual glacial ice encounter frequency with the installation in consideration.

Note that the above conditions are correlated and site-specific.

3.2 Glacial ice in the Barents Sea

3.2.1 Source

The dominant source of glacial ice features in the Barents Sea is calving from the ice cliffs of Franz Josef Land. Most calving occurs in the late summer and autumn (June through September). The number of glacial ice features close to the calving sources is higher in winter than in summer (Løset et al., 2006). Figure 1 shows the major sources of glacial ice features in the Barents Sea. The main ocean currents are also depicted in the figure with red indicating relatively warm water, grey indicating slightly colder water, and blue for cold Arctic water.

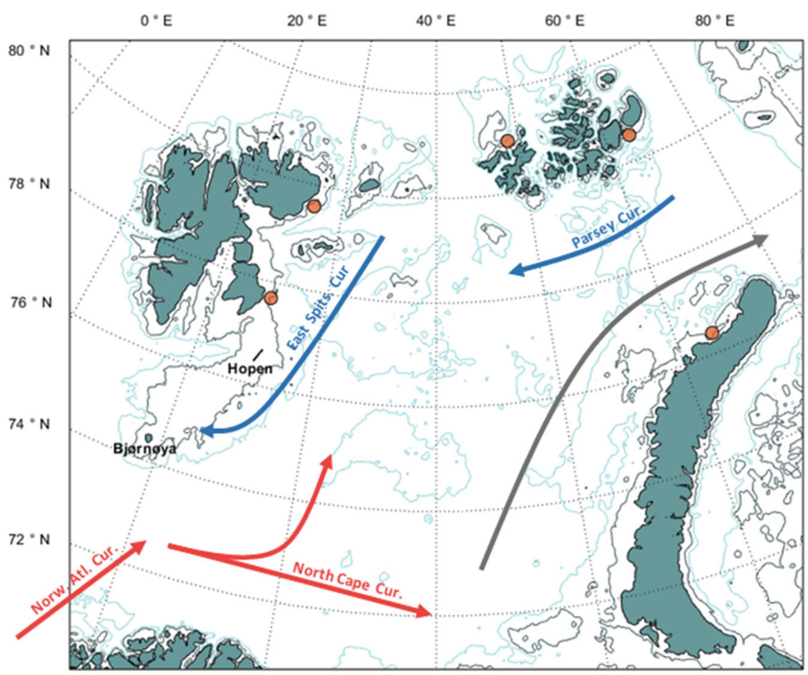

Figure 1. Major sources of iceberg production in the Barents Sea (orange-filled circles) and the main ocean currents. Light and green contour lines are the isobaths at 100 and 200 m, respectively.

Table 1 provides estimates of the annual discharge rate from the major sources of glacial ice features in the Barents Sea.

Table 1. Major iceberg calving locations and rates in the Barents Sea.

Geographical area	Calving location	Discharge rate (km^3/year)	Data source
Franz Josef Land (Eastern side)	80.5°N/62.8°E	2.64	(Kubyshkin et al., 2006)
Franz Josef Land (Western side)	81.0°N/48.7°E	1.76	(Kubyshkin et al. 2006)
Nordaustfonna	79.6°N/27.0°E	2.7	(Dowdeswell et al., 2008)
Edgeøya	77.7°N/25.0°E	0.6	(Hagen et al., 2003)
Novaya Zemlya	76.4°N/63.0°E	1.0	(Kubyshkin et al. 2006)

The percentages of the discharge rates indicated in Table 1 that would result in birth of icebergs ready to drift into the Barents Sea is highly uncertain and currently the data available to estimate these percentages are limited. This is one of the main sources of uncertainty when glacial ice conditions are to be determined from numerical simulations (refer to Section 3.3.2). In lieu of accurate data, one may use the estimates in Table 2 as input to numerical simulations for the determination of glacial ice conditions. The numbers in Table 2 are based on AARI (2005) and Abramov (1996) and they assume that the five major sources of glacial ice features in the Barents Sea would yield their maximum production of icebergs simultaneously.

Table 2. Major iceberg calving locations and average iceberg production rates in the Barents Sea.

Geographical area	Estimated number of icebergs released/year
Franz Josef Land (East)	76
Franz Josef Land (West)	169
Nordaustfonna	14
Edgeøya	17
Novaya Zemlya	49
Total	325

3.2.2 Iceberg mapping

The first well-documented iceberg study in the Barents Sea was the multi-sensor ice data acquisition programme ICEBASE (Sea Ice Investigations in the Barents Sea), which was funded by BP Norway, Esso Norway and Mobil Exploration Norway. The campaign was executed during mid-winter and fall 1987, and the main purpose was to obtain comprehensive information about sea ice and icebergs in the Barents Sea (Løset and Carstens, 1996). The specific elements of the acquisition programme were precision stereo aerial photography, helicopter-borne impulse radar, satellite imagery, airborne synthetic aperture radar and three ground truthing field campaigns. Important findings from the ICEBASE acquisition programme are summarised below:

The global geometry of an iceberg can be characterised by a shape factor (S_{peri}) and a sail volume shape factor (S_{sail}), expressed in Eqs. (1) and (2) respectively.

$$S_{peri} = \frac{4\pi A}{p^2} \tag{1}$$

where A is the cross–sectional area at the waterline plane and p is the perimeter at the waterline. It is worth noticing that S_{peri} = 1 for a circle, 0.785 for a square and decreases for elongated shapes.

$$S_{sail} = \frac{V_{sail}}{H_{\max} L_{\max} W_{\max}} \tag{2}$$

where V_{sail} is the above sea level volume, H_{max} the maximum sail height, L_{max} the maximum length. The maximum width (W_{max}) of an iceberg is measured perpendicular to L_{max}.

The maximum height H_{max} and length L_{max} of the icebergs are fitted to a 3-parameter Weibull probability distribution given by:

$$f(x) = \frac{\gamma}{\theta}\left(\frac{x-\varepsilon}{\theta}\right)^{\gamma-1} \exp\left[-\left(\frac{x-\varepsilon}{\theta}\right)^{\gamma}\right] \tag{3}$$

Where $x(>\varepsilon)$ is the statistical variable, ε the location parameter, $\theta > 0$ the scale parameter and $\gamma > 0$ the shape parameter. The corresponding cumulative function is given by:

$$F(x) = 1 - \exp\left[-\left(\frac{x-\varepsilon}{\theta}\right)^{\gamma}\right] \tag{4}$$

The location-, scale- and shape parameters of the Weibull distribution are shown in Table 3.

Table 3. Estimator values for the Weibull parameters (Løset and Carstens, 1996).

Parameter	Location, ε	Scale, θ	Shape, γ
H_{max}	4.5	13.0	1.45
L_{max}	44.9	74.4	0.83

ICEBASE became a model for its successor, the Ice Data Acquisition Programme (IDAP). IDAP was conducted by the OKN ("Operator Committee North of 62°N") over a five-year period from 1988-1992 (Spring et al., 1993, Spring, 1994). The data from the IDAP acquisition programme provided average iceberg size characteristics of 91 m×64 m×15 m for the length, width and sail height, respectively. The iceberg length and width distributions from IDAP are typically used as input data for iceberg drift models in the Barents Sea (Hansen et al., 2019, Keghouche et al., 2010). However, the locations of the icebergs observed during the IDAP campaign were generally not close to any of the iceberg-producing glaciers. Moreover, it may be questionable that the distribution derived from the IDAP data would be valid at different sources. Table 4 shows the parameters of the Weibull distribution of iceberg length based on the IDAP data. The table shows also the relationships between the main dimensions of icebergs that are often used in the numerical simulations of iceberg conditions.

Table 4. Typical input parameters for the birth of glacial ice features.

Iceberg parameters		Input value			Data source
Length	L_i	Weibull distribution			IDAP
		Location	Scale	Shape	
		30.1	64.97	1.15	
Width	W_i	$W_\mathrm{i} = 0.7 \cdot L_\mathrm{i} \cdot \exp(-0.00062 \cdot L_\mathrm{i})$			(Dezecot and Eik, 2015)
Total height (sail + keel)	H_i	$H_\mathrm{i} = 0.3 \cdot L_i \cdot \exp(-0.00062 \cdot L_i)$			(Dezecot and Eik, 2015)
Mass	M_i	$M_\mathrm{i} = H_\mathrm{i} \cdot L_\mathrm{i} \cdot W_\mathrm{i} \cdot \rho_\mathrm{i}$			-

3.2.3 Physical properties

Glacier ice develops from successive snowfalls of pure freshwater snow which compresses under its own weight until they become solid ice. The initial density of freshly precipitated snow is about 400 kg/m^3, but the density (ρ_i) increases with depth and overburden pressure, reaching about 600 kg/m^3, at depth 10 m below surface (Sanderson, 1988). At depth 50 m the density reaches about 820 kg/m^3.

The ice temperature in the central region of an iceberg is almost unaffected by the thermal conditions imposed on its boundary owing to the insulation quality of the ice. When correlated with glacioclimatic conditions, this temperature conservation at a minimum 12 m distance from the iceberg boundary may be used to backtrack an iceberg to its parent ice cliff (Løset, 1993).

The strength of iceberg ice has been measured in just a few occasions in the Barents Sea with mostly uniaxial compression tests at a strain rate of $10^{-3}s^{-1}$. The IDAP laboratory testing from 1988 provided a mean value for compressive strength of 5.4 MPa and a range from 2.3 MPa to 7.3 MPa for 16 tests at -10°C (Spring et al., 1993). Additional data, taken in 1990, had a mean of 2.3 MPa and a range from 1.6 MPa to 3.8 MPa for 7 tests at -4°C.

Table 5 shows results from an in-situ test from a small pinnacle iceberg (about 40 m across and 7 m sail height) located at about 77°N, 29°E North-East of Hopen in May 2009 (UNIS, 2009). The ice temperature was high, and the tests yielded an average strength of 2.8 MPa. For larger icebergs in a melting stage, Løset (1993) has shown that the iceberg temperature at about 2.5-3 m inward from the ice surface will reflect the core temperature of the iceberg. This means that colder ice can be expected further into the ice which again increases the strength of the iceberg ice and may switch the failure mode from ductile to brittle failure of the ice. This information is relevant to studies of impacts between glacial ice features and structures.

However, it is still an open question on how to relate the in-situ compressive strength to an appropriate ice material model. In most practical applications, the numerical ice material model is often calibrated against the process pressure-area (P-A) curves or the force-area relationship described in Annex B .5.5.2.

Table 5. Strain rate $10^{-3}s^{-1}$. Uniaxial compressive strength.

Depth from the top iceberg surface (cm)	Temperature (°C)	Uniaxial compressive strength (MPa)
23-49	-2.1	
131-169	-1.9	1.2
169-189	-3.3	2.3
189-210	-1.4	5.5
210-240	-1.3	4.1
292-325	-3.5	1.0

3.3 Glacial ice probability of intrusions and encounter frequency

3.3.1 Arctic iceberg atlas

The Atlas of Arctic Icebergs (Abramov, 1996) provides contour lines of annual probability of occurrence of icebergs in the Arctic seas. The Atlas is usually helpful for early evaluation of iceberg presence. The main bulk of the Atlas data are from aerial surveys (around 96% of the iceberg data were obtained from ice reconnaissance flights; around 4% from shipboard observations; and less than 0.1% were obtained by other means, e.g., observations at coastal polar stations, satellite observations). Different Arctic seas had different duration of iceberg observations and the longest history of observations was in the Barents Sea.

The Abramov Atlas provides charts of iceberg annual occurrence probability. In order to develop these charts, the Atlas assumes uniform distribution of icebergs within the region of observation and expands the estimate of the frequency of icebergs along the flight route into 100 × 100 km cells. By sorting the observations in each cell per month and accumulating the observations over years, the Atlas provides charts for monthly and annual occurrence probabilities. The Atlas calculates the probability of iceberg occurrence as:

$$P = \frac{100m}{n} \tag{5}$$

where *P* is the probability of iceberg occurrence (%), *m* is the number of years where icebergs occurred in the given cell in the given period of time, and *n* is the total number of years of observations for the given cell in the given period of time. Figure 2 shows the chart of annual probability of occurrence of icebergs as presented in the Atlas.

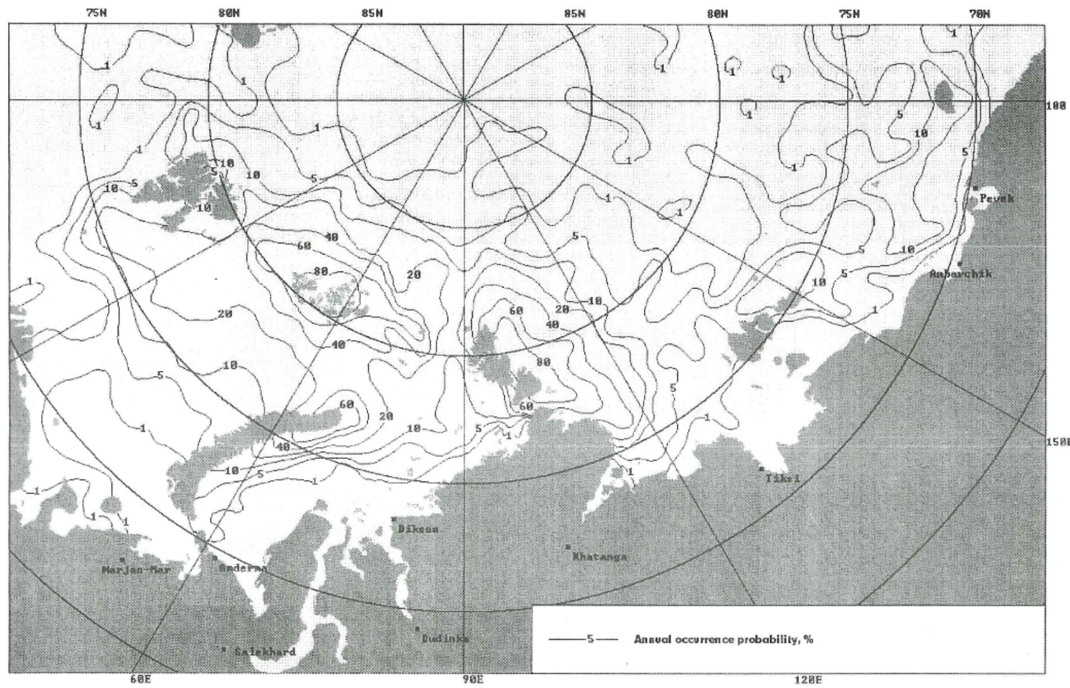

Figure 2. Annual probability of occurrence of icebergs, from The Atlas of Arctic Icebergs (Abramov, 1996).

Note that that the Abramov Atlas will most likely underestimate the annual probability of occurrence of icebergs in the Western part of the Barents Sea. The Abramov Atlas does not give any indication about the frequency of scouting missions in this area and it can be only concluded that they were not very frequent.

3.3.2 Numerical simulations of annual glacial ice encounter frequency

Field mapping/measurements should always be favoured when deriving a credible annual glacial ice encounter frequency E_N by the structure of interest at a specific site. However, such full-scale data are often scarce and limited. Therefore, statistical information of the geometry, drift velocity and encounter frequencies of glacial ice may alternatively be obtained by simulating the global and local drift.

The simulation model should include the dominant sources (see Section 3.2.1) of drifting glacial ice features in the Barents Sea that are of relevance to the site being developed. The annual iceberg production rates from these sources can be estimated based on theoretical calculations of precipitation rates and adjusted based on observations/experience from the region (e.g., see Table 2).

In the numerical simulation model, the glacial ice features can be released randomly in time and space applying uniform probability distributions. The releases should take place from July 1st until November 30th and be distributed randomly in polygonal areas along the sources. The geometrical form and the thermomechanical properties of the released icebergs may be derived based on statistical data from the ICEBASE and IDAP measurement programmes (e.g., refer to Table 4).

The simulation model should include a global and a local model. For the global iceberg drift model, environmental forces such as wind force, current force, Coriolis force, mean wave drift force, and potential neighbouring sea ice forces should be included. Along the drift path, glacial ice deterioration due to wave and thermal erosions should be accounted for; many small glacial features will not survive a drift further south. The results of the global model should be processed to create contour lines on a map of the Barents Sea showing the annual probability of occurrence of icebergs in a local domain of e.g., 100 × 100 km. More information on the global modelling can be found in Annex A .2.

Given the mass/size distribution of the icebergs that are predicted to enter the local domain of 100 × 100 km from simulations with the global model, more detailed simulations with a local model that takes into account the installation's size (e.g., 100 × 100 m) shall be performed. More information of the local modelling can be found in Annex A .3.

The global and local model together yield information on the encounter frequency E_N, the size/mass and geometry distribution, and the mean drift velocity V_i of the glacial ice features impacting the installation.

4 Glacial Ice Actions

4.1 General

A probabilistic approach should be applied in order to identify actions corresponding to 10^{-2} exceedance probability level (see Eq. (7)). In the early phase, a deterministic method may be applied, in which extreme (e.g. mass or kinetic energy) and nominal values (e.g. compression strength) of glacial ice features are combined to yield ULS. Further requirements and guidance are found in ISO 19906 and in Jordaan et al. (2014) .

Abnormal ice actions corresponding to certain exceedance probability level (see Eq. (8)) shall be characterized by the kinetic energy (mass and relative impact velocity) of the glacial ice feature and shall be determined in a risk analysis, see NORSOK Z-013. The risk analysis shall consider both the mean drift motion (including weathering) and the oscillatory motion of the glacial ice feature. The effect of glacial ice feature size on the ALS impact energy shall be investigated.

When estimating actions from glacial ice features, it shall be taken into account that larger glacial ice features are more likely to impact a structure than smaller ones and those moving faster are more likely to encounter the structure than the slower. Reason for this is that they will swipe larger areas and thus statistically be more likely to impact. This can be taken into account by updating parent distributions prior to response analysis.

4.2 Mean drift motion and encounter frequency

The mean drift motion V_i and encounter frequency E_N of glacial ice features are calculated in the global and local models described in Section 3.3.2. In the analyses, the following information shall be established:

- Mass/size (length and width) distribution of the potentially encountered glacial ice features.
- The mean drift velocity V_i of the glacial ice features of varying mass/sizes.
- Encounter frequency E_N of glacial ice features of varying mass/sizes.

The modelling details are presented in Section 3.3.2 and Annex A.

4.3 Oscillatory motion and impact velocity

The wave-driven oscillatory motions of the glacial ice feature should be calculated. The oscillatory motion is combined with the mean drift motion to trace the trajectory of a glacial ice feature. For a given trajectory, the method developed by Fylling (1994) for ship collision and later extended by Lu and Amdahl (2019) for glacial ice impacts can be employed to sample impact events and their associated impact velocity distribution V_{impact} . In the analyses, the dependence of the impact velocity on the following parameters should be established:

- Mass/size of the glacial ice features.
- Wave, wind, and current conditions.

Calculation details to establish $V_{impact}(M\text{ , wave conditions,}V_i)$ are presented and exemplified in Annex B .4.

4.4 Kinetic energy of an ice impact event

For an individual glacial ice impact action, the impact energy to be dissipated as deformation energy in the structure and ice is a fraction of the kinetic energy E_k^V of the incoming glacial ice feature relative to the structure (see Eq. (6)).

$$E_k^V = \frac{1}{2}(M + A)(V_{impact})^2 \tag{6}$$

where, *M* and *A* are the mass and added mass of a given glacial ice feature. V_{impact} is the impact velocity, which depends upon the mean drift velocity as well as the oscillatory wave induced velocity. In Eq. (6), the statistical distribution of *M* is site specific. The distribution of mass and geometry; and the encounter frequency E_N can be obtained either from credible field measurements or numerical simulations (refer to Section 4.2). With known statistical distribution of *M, A*, and the derived distribution of V_{impact}, the cumulative distribution function $F_V(E_k)$ of individual ice actions can be established through Eq. (6).

4.5 Probabilistic approach for ice events analysis

In accordance to ISO19906 (2019), the design kinetic energy E_k^{design} with the corresponding exceedance levels are presented in Eqs. (7) and (8), in which, P is a probability, subscripts E refers to EL and A refers AL, E_k^Z is the annual maxima of the kinetic energy of glacial ice features' impact events.

$$\mathrm{P}(E_k^Z > E_{k,E}^{design}) = 10^{-2} \tag{7}$$

$$\begin{aligned} \mathrm{P}(E_k^Z > E_{k,A}^{design}) &= 10^{-4} \text{ (for L1 structures)} \\ &= 10^{-3} \text{ (for L2 structures)} \end{aligned} \tag{8}$$

L1 and L2 structures in Eq. (8) are determined in accordance to the process set out in ISO 19900:2013, 6.4 to characterise a structure's exposure level. All manned, non-evacuated platforms and high-consequence platforms or structures are designated L1; unmanned, low-consequence platforms or structures are designated L3; other platforms or structures are designated L2. The cumulative distribution function $F_Z(E_k)$ of the annual maxima E_k^Z can be related to the cumulative distribution function $F_V(E_k)$ of ice actions through Eq. (9) with known encounter frequency E_N.

$$F_Z(E_k) = \exp\{-E_N[1 - F_V(E_k)]\} \tag{9}$$

Afterwards, the corresponding design kinetic energy can be obtained through Eqs. (10) and (11) with equivalence to Eqs. (7) and (8).

$$F_Z(E_{k,E}^{design}) = 0.99 \tag{10}$$

$$\begin{aligned} F_Z(E_{k,A}^{design}) &= 0.9999 \text{ (for L1 structures)} \\ &= 0.999 \text{ (for L2 structures)} \end{aligned} \tag{11}$$

4.6 Assessment of installation damage

4.6.1 Damage assessment method

Generally, a substantial part of the kinetic energy $E_{k,A}^{design}$, i.e. the impact energy, corresponding to the ALS design criteria must dissipated through structural and ice deformations.

Analysis of impact energy and analysis associated structural damage/deformation can either be coupled or decoupled. The methods can be classified as 'fully/partially coupled' or 'decoupled'. Details of some of the methods are presented in Annex B .1.

The structural damage should as far as possible take the interactive nature of the structure and ice deformation, so as to reflect all the possible deign principles (refer Annex B .2).

4.6.2 Geometry of glacial ice features

The shape of the glacial ice is characterised by a global and local geometry.

4.6.2.1 Global geometry

The global geometry information (in terms of length, width, and height) can be obtained from the glacial ice condition analyses (refer to Sections 3.2.2 and/or 3.3.2) and is important with respect to identification of locations exposed to impacts and the amount of energy that must be dissipated as deformation/strain energy in the ice and the installation.

4.6.2.2 Local geometry

The local geometry influences the distribution of damage in the installation and deformation of the ice. Without any statistical information on the local geometry of glacial ice features or agreed characteristic local shape, it is alternatively recommended to identify a critical local geometry that for a given impact energy maximizes a certain damage to the installation. The damage is typically penetration into the structure with possible flooding of void spaces, but other damage criteria may apply, e.g. denting that jeopardises the residual strength.

The calculation of the critical local geometry is influenced by:

- Structural scantlings and strength.
- Failure criteria of the steel material.
- Ice material model including relevant failure processes.
- The amount of impact energy to be dissipated.

The general trend is that sharp local ice geometries tend to deform with little structural damage; while blunt local ice geometries deform little but inflict structural damage over a large contact area.

The objective of the design process is thus to minimize the ‘maximum structural damage/deformation’ for a given impact energy when it is subjected to impacts from ice with the identified critical local geometry.

Annex A Glacial ice condition modelling

Annex A .1 Birth of glacial ice features

The amount of iceberg-producing calving from an ice margin is influenced by the mass balance of the glacier, the crevassing within the glacier, by the rate of glacier flow, by whether the glacier terminus is grounded or afloat, and therefore by the depth of water fronting the ice. The principle is sketched in Figure 3 and Figure 4.

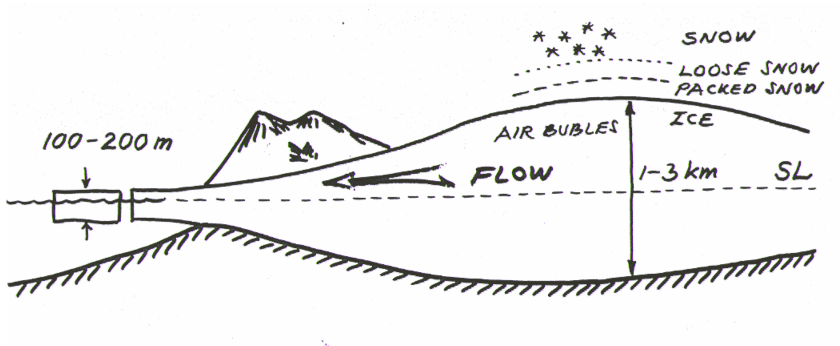

Figure 3. Principle sketch of the formation process of glaciers and icebergs (Løset et al., 2006).

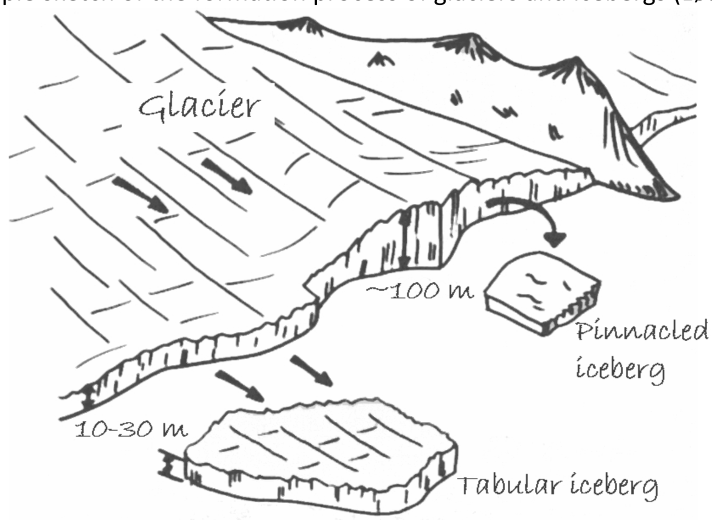

Figure 4. Sketch of the formation process of tabular and irregular icebergs from an ice cliff (Løset et al., 2006).

The dominant source of icebergs in the Barents Sea is calving from the ice cliffs of Franz Josef Land. This archipelago consists of about 2600 km of tidewater ice cliffs (Løset, 1993). The fjords and adjacent waters are rather deep, typically 100 – 200 m deep, which may allow large icebergs to escape from the glacier terminus. Most calving occurs in the late summer and autumn (June through September), when ocean wave excitation reaches the calving ice cliffs. Iceberg drift is very restricted in winter due to sea ice. The number of icebergs close to the calving sources is higher in winter than in summer (Løset et al., 2006).

Annex A .2 Global model

Annex A .2.1 Glacial ice drift

The equation for iceberg drift motion, is given by:

$$m \cdot (1 + C_m)\frac{dV_i}{dt} = F_a + F_w + F_c + F_{wd} + F_{si} \quad (12)$$

where m is the iceberg mass, C_m is the added mass coefficient, V_i is the iceberg velocity, F_a and F_w are the air and current form drag, respectively, F_c is the Coriolis force, F_{wd} is the mean wave drift force and F_{si} is forcing from sea ice. Note that forces due to ocean tilt are assumed to be marginal in this large-scale model and thus neglected. All the force terms are defined in the following and they are based on Eik (2009) and references therein, unless stated otherwise. The added mass is set to zero in this study due to the lack of data and due to the considerable uncertainty in the available estimates of icebergs' mass.

The drag force due to current is expressed as:

$$F_w = \frac{1}{2} \cdot \rho_w \cdot C_w \cdot A_w \cdot |V_w - V_i|(V_w - V_i) \quad (13)$$

where ρ_w is the density of the sea water, C_w the current form drag coefficient, V_w is the current speed and A_w is the cross-sectional area on which the current velocity acts. We adopt the approach of Wagner et al. (2017) and define A_w as:

$$A_w = \frac{\rho_i}{\rho_w} \cdot \frac{2}{\pi} \cdot (L_i + W_i) \cdot H_i \quad (14)$$

where ρ_i is the density of glacier ice. L_i, W_i and H_i are the iceberg length, width and total height (sail plus keel), respectively.

The drag force due to wind is expressed as:

$$F_a = \frac{1}{2} \cdot \rho_a \cdot C_a \cdot A_a \cdot |V_a - V_i|(V_a - V_i) \quad (15)$$

where ρ_a is the density of the air, C_a the air form drag coefficient, V_a the wind velocity and A_a the cross-sectional area on which the wind velocity acts. This area A_a is defined as (Wagner et al., 2017):

$$A_a = \frac{\rho_w - \rho_i}{\rho_i} \cdot A_w \quad (16)$$

The Coriolis force reads:

$$F_{cor} = -m \cdot f \times V_i \quad (17)$$

where f is the Coriolis parameter, which can be written as:

$$f = 1.45 \cdot 10^{-4} \cdot \sin(\varphi)\ \mathrm{k} \quad (18)$$

where φ is the geographic latitude position, and k is a unit vector in the vertical (up) direction. Note that the iceberg velocity, V_i, has two components, i.e., east and north.

The expression for the wave drift force is

$$F_{wd} = 0.25 \cdot \rho_w \cdot g \cdot a^2 \cdot L_i \cdot \frac{V_{wa}}{|V_{wa}|} \quad (19)$$

where a is the wave amplitude ($a = 0.5 \cdot H_s$, where H_s is the significant wave heigth) and $\frac{V_{wa}}{|V_{wa}|}$ is the wave direction.

The expression for the sea ice force is

$$\begin{aligned} F_{si} &= 0 && : C_i \leq 0.15 \\ F_{si} &= 0.5 \cdot \rho_{si} \cdot C_{si} \cdot A_{si} \cdot |V_{si} - V_i| \cdot (V_{si} - V_i) && : 0.15 \leq C_i \leq 0.9 \\ F_{si} &= -(F_a + F_w + F_{cor}) && : C_i \geq 0.9 \,\&\, h > h_{min} \end{aligned} \tag{20}$$

where ρ_{si} is the density of sea ice, C_{si} the sea ice drag coefficient, V_{si} the sea ice drift, C_i the ice concentration, *h* the sea ice thickness, h_{min} is the minimum sea ice thickness to lock an iceberg in the sea ice and A_{si} is the cross-sectional area on which the sea ice acts and is defined as:

$$A_{si} = \frac{2}{\pi} \cdot (L_i + W_i) \cdot h \tag{21}$$

The minimum sea ice thickness (h_{min}) reads:

$$h_{min} = \frac{P}{P^* \cdot exp(-20 \cdot (1 - C_i))} \tag{22}$$

where P is the sea ice strength and P^* is a sea ice coefficient.

Annex A .2.2 Glacial ice deterioration

The iceberg length, width and total height deteriorate with the following rates:

$$\frac{d(L_i)}{dt} = \frac{d(W_i)}{dt} = -(M_e + M_v) \tag{23}$$

$$\frac{d(H_i)}{dt} = -M_b \tag{24}$$

It is considered that the melt and erosion of an iceberg is mainly driven by wave erosion M_e, bottom melt M_b and buoyant convection at the side walls M_v. In the following, we summarise the formulation of these three terms. All the melt terms given here have units of metres per day. Further details and references can be found in the paper by Martin and Adcroft (2010). Wave erosion is given by:

$$M_e = \frac{1}{12} S_s \left(1 + cos\left(\pi A_i^3\right)\right)\left(\tilde{T}_o + 2\right) \tag{25}$$

where S_s is the sea state, A_i is the fractional sea ice cover and $\tilde{T}_o$ is the sea surface temperature. Sea state S_s is estimated by a fit to the Beaufort scale:

$$S_s = \frac{3}{2}|V_a - V_w|^{1/2} + \frac{1}{10}|V_a - V_w| \tag{26}$$

Melt rate at the base of the iceberg due to the turbulence created by the relative motion of water passing the iceberg is given by:

$$M_b = 0.58|V_i - V_w|^{0.8} \frac{\tilde{T}_o - \tilde{T}}{L_i^{0.2}} \tag{27}$$

where $\tilde{T}$ is the effective iceberg temperature assumed to be constantly at -4 °C.

The melt rate due to buoyant convection along the side walls of the iceberg caused by the temperature contrast between the iceberg and the ocean. This melt is given by:

$$M_v = 7.62 \cdot 10^{-3}\tilde{T}_o + 1.29 \cdot 10^{-3}\tilde{T}_o^2 \tag{28}$$

Finally, hydrostatic stability of the iceberg is considered by allowing for icebergs to capsize when the width-to-height ratio $\varepsilon \equiv W_i/H_i$ falls below a critical value ε_c. The criteria for the critical value is derived as:

$$\varepsilon_c = \sqrt{6\frac{\rho_i}{\rho_w}\left(1 - \frac{\rho_i}{\rho_w}\right)} \tag{29}$$

Detailed meteorological data source and relevant parameters' inputs of the model can be referred in the report (Lu et al., 2019).

Annex A .3 Local model

Annex A .3.1 Glacial ice drift

The basic equation in the local model is given by:

$$m \cdot (1 + C_m)\frac{d}{dt}\left(V_i - V_g - V_t\right) = F_a + F_w + F_c + F_{wd} + F_{si} \tag{30}$$

where m is the iceberg mass, C_m is the added mass coefficient, V_i is the iceberg velocity, V_g is the geostrophic current, V_t is the tidal current, F_a and F_w are the air and current form drag, respectively, F_c is the Coriolis force, F_{wd} is the mean wave drift force and F_{si} is the sea ice drag. Assuming that the Coriolis force acting on the sea water will be balanced by the sea surface tilt (in the absence of wind). The formulae to calculate drag forces are the same used in the global model.

Annex A .3.2 Glacial ice deterioration

The deterioration equations of the local model are identical to the ones used for the global analysis. The equations are given in Eqs. (23) to (29).

Annex A .3.3 Sources and size distribution icebergs

A sufficient number of icebergs (typically about 100 icebergs) shall be generated from the statistical distributions derived from the global model. The initial (start) time for each of the icebergs is random following a uniform distribution over the past 27 years.

Annex A .3.4 Collision risk

The approach presented by Mathiesen et al. (1992) to estimate the risk collision between an iceberg and e.g., a 100 × 100 m structure at a given site can be adopted. The annual iceberg encounter frequency reads:

$$E_N = P_l \cdot N \tag{31}$$

where E_N is the number of icebergs colliding with the structure per year, P_l is the local probability of collision (derived from the local model), and N is the expected number of icebergs entering the given site per year (derived from the global model).

The local probability of collision is calculated from the local model as follows:

For each iceberg,

1. The spatial domain of e.g., (100 × 100 km) is subdivided into smaller boxes or windows of size *l* x *l*.
2. The number of boxes that contain a part of the iceberg track is counted.
3. The above two steps are repeated for decreasing box sizes.
4. The number of boxes that contain part of the iceberg track, *N(l),* are plotted versus the window size, *l*, on a log-log scale.

For all icebergs,

5. Combine the log (*N(l)*) versus log *(l)* curves for all icebergs in one plot and find the curve that represents weighted average of all curves.
6. Fit the curve resulted from Step 5 to estimate the fractal dimension (*D*), the constant (*C*) and the scaling factor (l_0) in Equation (32).

$$N(l) = C\left(\frac{l}{l_0}\right)^{-D} \tag{32}$$

7. Finally, the local probability P_l, is computed as:

$$P_l = \frac{C}{k} \cdot \left(\frac{l}{l_0}\right)^{2-D} \tag{33}$$

where $k = \frac{(100 \cdot 100)}{{l_0}^2} = 10000.$

Detailed meteorological data source and relevant parameters' inputs of the model can be referred in the report (Lu et al., 2019).

Annex B Annex B Glacial ice impacts and damage assessment

Annex B .1 General

The requirement and methods given in this section are generic although the major knowledge was developed for impacts with small glacial ice features with waterline lengths of around 15-30 m. It is important to consider these small glacial ice features due to the difficulties in detecting and managing them (Lu et al., 2019). In addition, although small ice features have less mass compared to icebergs, they have larger wave-driven motions that may cause larger impact velocities. The information of the size and shape of glacial ice features is site-specific. The encounter frequency of glacial ice features together with their size/mass statistics for a given site can be obtained by means of field measurements or numerical modelling (refer to Section 4.2).

It is also necessary to perform simulation of the relative motion between the glacial ice feature and the installation so as to determine the impact range and impact velocity's distributions described in Section 4.3.

Depending upon the impact conditions, a part of the kinetic energy may be retained after impact. The difference between the kinetic energy before and after impact constitutes the demand for strain energy dissipation in the installation and in the ice. The energy that needs to be dissipated as strain energy may be determined in an *external mechanics* analysis. The proportion of strain energy that is dissipated by structural deformation and ice deformation, respectively, is determined in the *internal mechanics* analysis.

In the *internal mechanics*, the *local* structural lay-out and dimensions of the installation as well as the *local* geometry of the ice feature in the contact area are important. A critical local ice shape which maximizes the damage to the installation for a given demand for strain energy dissipation needs to be determined. The damage in consideration will normally be penetration and puncturing of the structure causing flooding of void spaces and loss of stability at risk, but other criteria may be envisaged; e.g. residual strength of the damaged installation. The critical shape depends upon the ice strength as well as the local structural lay-out and dimensions in the contact area.

The damaged structure after ice impacts shall be able to resist relevant permanent and variable actions in a metocean condition corresponding to annual exceedance probability of 10^{-2}.

Methods for the assessment of structural effects from ice impacts may be categorized as follows:

1. Fully-coupled non-linear dynamic finite element (or equivalent methods) analyses of ice impacts accounting for interactive nature of the structural and ice strain energy dissipation in the contact area as well as the global motions.
2. Partially-coupled analyses of ice impacts accounting for the interaction effects as considered in fully coupled analyses. The effect of ice structure interaction is, however, partially considered by adopting simplified expressions for ice damage and structural deformation
3. Decoupled analysis where the *external* and *internal mechanics* are calculated independently. The strain energy dissipation (i.e., the internal mechanics part) can be calculated using:
   a) Nonlinear finite element analysis with realistic ice structure interactions
   b) simplified methods with uncoupled or partially coupled structural deformation and ice damage

Requirements to the use of the various methods are described in Annex B .5.1 (Method 1), Annex B .5.2 (Method 2), Annex B .5.5.2 (Method 3a), and Annex B .5.5.1 (Method 3b).

Whenever non-linear dynamic finite element analysis is applied to analyse the structural deformations, all effects described in Annex B .5.5 and Annex B .6 shall either be implicitly covered by the modelling adopted or subjected to special considerations, whenever relevant. Practical guidance on how to establish structural resistance analysis by the use of non-linear finite element methods is given in DNV-GL RP-C208 *Determination of Structural Capacity by Nonlinear FE analysis methods*

Annex B .2 Design Principles

With respect to the distribution of strain energy dissipation, there may be distinguished between, see Figure 5:

- strength design
- ductility design
- shared-energy design

Strength design implies that the installation is strong enough to resist the impact force with minor deformation, so that the ice is forced to deform and dissipate the major part of the energy. This is typically the checks carried out in ULS.

Ductility design implies that the installation undergoes large, plastic deformations and dissipates the major part of the impact energy.

Shared energy design implies that both the installation and ice contribute significantly to the energy dissipation.

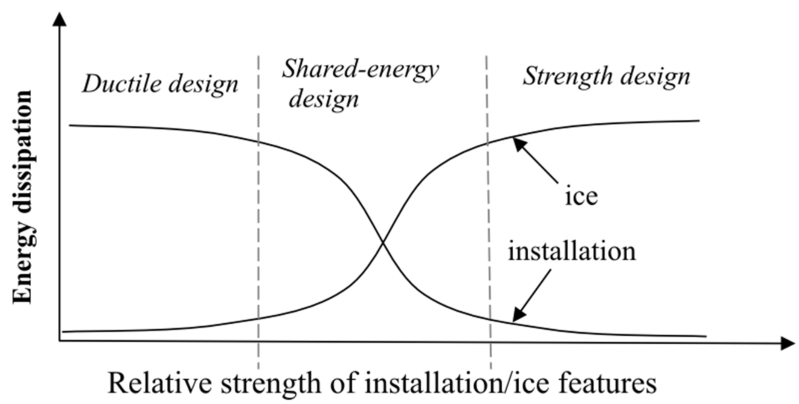

Figure 5. Energy dissipation for strength, ductile and shared-energy design.

From calculation point of view, strength design or ductility design is favourable. In this case the energy dissipation in the installation or ice, whichever is 'softer', can be calculated on the basis of the geometry of the 'strong' body. In the shared energy design, both the magnitude and distribution of the impact force depends upon the deformation of both bodies. This interaction makes the analysis more complex.

In most cases, ductile or shared energy design is used. However, strength design may in some cases be achievable with little increase in steel weight. It is noticed that strength design is in principle identical to ULS design; the installation has to resist the pressure and forces generated by the deforming ice.

Often the transition range of the relative strength from predominantly ductile behaviour to strength behaviour is relatively narrow, where a slight increase of installation strength may substantially reduce its contribution to the damage and energy dissipation.

For simplicity, ductile design principles may be adopted for local geometries that are equal to or blunter than the critical geometry of the glacial ice feature, see Annex B .3, i.e. the ice is considered to be rigid.

Annex B .3 Ice Geometry

The ice shall be described by a global geometry and a local geometry (see Figure 6). The global geometry is decisive with respect to identification of areas exposed to impacts and to the outcome of the external mechanics analysis in Annex B .5.4. The local geometry is needed for the internal mechanics analysis, see Annex B .5.5.2.

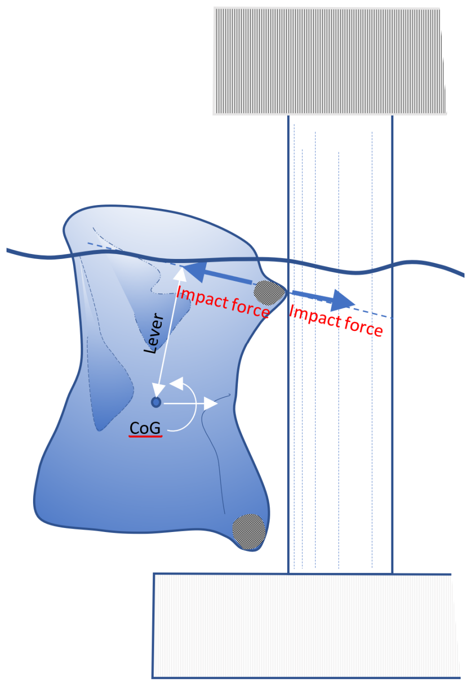

Figure 6. Illustration of the local and global geometry of a glacial ice for potential impact against a column or a pontoon. The grey areas indicate regions where local geometry must be described.

The local and global geometry shall be representative for actual impacting glacial ice features. Various local and global geometries shall be examined to determine the critical geometry that maximizes the damage to the installation.

If the distribution of local geometry is not sufficiently known, the critical local geometry should be found as follows:

- The local geometry is described by a radius of curvature. The shapes with the smallest radius of curvature will be crushed, while the shapes with the largest radius of curvatures will deform the platform, but with moderate ice crushing. The critical geometry is the radius of curvature that for a given impact energy maximizes the *penetration* into the installation. It is based upon the assumption that penetration that may lead to flooding of empty compartments or spill from cargo tanks, is critical. If other failure modes are considered more relevant (e.g. the residual strength of damaged members), the critical shape must be searched with respect to these criteria.

The critical geometry of ice depends on the ice strength as well as the dimensions and strength of the installation in the contact area. In lieu of more accurate calculations, the critical ice geometry may be assumed to be spherical in the contact area with a sphere radius - panel length ratio equal to 0.8. Unless otherwise assessed with advanced calculations, glacial ice with local geometries sharper than this critical geometry shall be considered to be significantly crushed by the structure. Refer Commentary section Annex B .8.1 for idea behind the critical sharpness of local ice geometry.

Annex B .4 Ice Impact Velocity and Kinetic Energy

In Eq. (6), calculating the kinetic energy E_k^V for individual impacts requires the distribution of the ice impact velocities V_{impact}. Each impact velocity corresponds to one of the sampled impact events; and the impact velocity consists of two components:

- A mean drift velocity V_i, induced by wind, wave and current.
- A wave-driven oscillatory velocity v_{cyclic}.

Before sampling the impact events and their associated V_i and v_{cyclic}, the time domain motion (or trajectory) of the glacial ice feature should be calculated. A decoupled approach to separately calculate the mean drift motion (see Annex B .4.1) and the wave-driven oscillatory motion (see Annex B .4.2) is possible.

The impact velocities V_{impact} depend on the mass/size of the glacial ice feature and wave conditions at a specific site. A complete construction and sampling between all possible combinations of M, V_i, v_{cyclic}, and wave conditions is ideal, but difficult. In lieu of such complete analyses, it is possible to make some simplifications (refer Commentary section Annex B .8.2)

Annex B .4.1 Mean drift motion

The method to calculate the mean drift velocity V_i is presented in Annex A. A joint distribution of V_i and *M* can be established in the calculation of the kinetic energy E_k^V in Eq. (6). The mean drift velocity V_i influences the impact events: as higher drift velocity tends to divert impact location towards higher locations and lower drift velocity leads to more evenly spread impact locations given the same oscillatory motions of the glacial ice features (Lu and Amdahl, 2019).

Annex B .4.2 Wave-driven oscillatory motion

Annex B .4.2.1 General

The distribution of impact velocity of glacial ice over the vertical areas of the installation shall be determined. This shall be obtained by simulating the motion of a drifting glacial ice feature relative to the installation at the instant of impact. The wave-driven oscillatory sway and heave motion of the glacial ice feature shall be considered, while the roll motion may be disregarded (especially for small glacial ice features). The motion may be based on CFD techniques or potential theory.

The following effects should at least be taken into account:

- Added mass and damping for the sway and heave motions.
- Buoyancy, Froude Krylov and diffraction forces. The effect of draft changes and submersion due to the heave motion shall be accounted for.

- Drag forces balancing the mean horizontal force shall be included.

The repellent force (change of added mass for the glacial ice feature) in the close proximity of the installation may be taken into account. Viscous forces generated when the glacial ice feature is close to impact may be taken into account if validated against experiments.

The probability distribution of impact velocity shall be simulated using the method developed by Fylling (1994) for a drifting supply vessel and the extended model by Lu and Amdahl (2019) for drifting icebergs that includes the vertical distribution as well.

Annex B .4.2.2 Formulations of the numerical model

In lieu of more advanced simulations, the 'simplified nonlinear model for wave induced glacial ice motion' developed in the project ST20_2019 (Lu et al., 2019) can be adopted. The formulations are mainly intended for small glacial ice features (refer Commentary section Annex B .8.2) and are summarised here.

Given the interaction model illustrated in Figure 7, the wave induced oscillatory motion for the glacial ice feature is determined with Eq. (34). Only the motion in the sway η_2 and heave η_3 directions are considered.

$$(A_{ij} + M)\ddot{\eta}_i + B_{ij}\dot{\eta}_i = F_i^W + F_i^R \quad (i = 2,3) \tag{34}$$

in which, M is the mass of the glacial ice feature. η_i is the displacement in i direction and $\ddot{\eta}_i$ and $\dot{\eta}_i$ the corresponding acceleration and velocity, respectively. A_{ij} and B_{ij} are the added mass and added damping of the glacial ice; together with the restoring force component F_i^R, which corresponds to the so-called radiation force components. On the right-hand side of Eq. (34), F_i^W is the wave excitation force. To calculate the motion η_i of a glacial ice in waves, the formulation of each force component is described below.

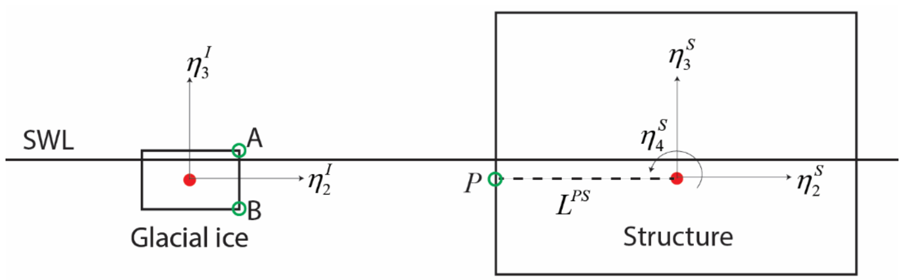

Figure 7. Interaction model and coordinate system.

The "small volume body in waves" assumption may be adopted. This means that the characteristic body size L and the wave length λ should satisfy the relationship of $\lambda / L > 5$ (Faltinsen, 1993). The wave excitation force F_i^W can be written in Eq. (35),

$$F_i^W = F_i^{FK} + F_i^{Diff} = -\iint_S p n_i ds + A_{i1}a_1 + A_{i2}a_2 + A_{i3}a_3 \tag{35}$$

in which, the Froude-Krylov force (Eqs. (36) and (37)) and diffraction force (Eq. (38)) can be formulated taking into account the instantaneous wetted volume (including full submersion).

$$F_i^{FK} = -\iint_S p n_i ds \tag{36}$$

$$p = \begin{cases} \dfrac{\rho g \zeta_a}{\omega} e^{kz} \sin(\omega t - kx) & z \le 0 \\ \dfrac{\rho g \zeta_a}{\omega} \sin(\omega t - kx) & z > 0 \end{cases} \tag{37}$$

where,

ρ	is the water density;
g	is the gravitational acceleration, 9.81 $\mathrm{m/s^2}$;
ζ_a	is the wave amplitude, in [m];
z	is the water depth calculated from the mean Still Water Level (SWL), in [m];
ω	is the wave frequency, in [rad/s];
k	is the wave number and can be expressed as $k = 2\pi / \lambda$.

For the general diffraction force expression F_i^{Diff} in Eq. (38), $A_{22}, A_{33}, A_{23}, A_{32}$, are the added mass coefficients of the glacial ice feature in sway, heave, sway/heave and heave/sway directions, respectively; whereas a_2 and a_3 are the undisturbed fluid particle acceleration at the geometric centre of the wetted volume in sway and heave directions, respectively (Faltinsen, 1993).

$$F_i^{Diff} = A_{i2} a_2 + A_{i3} a_3 \tag{38}$$

In Eq. (34), the restoring force F_i^R , by only considering the vertical direction motion η_3, can be formulated as in Eq. (39), in which, $D(S)$ is the distance from the centre of a discretised wetted area ds to the SWL. At static equilibrium in the absence of wave motion (i.e., $\eta_3 = 0$), it follows that, equivalently, $\rho g \int D(S) ds = Mg$, $F_3^R = 0$, and $(\rho g \int D(S) ds) / A_{WP} = \bar{D}$. $\bar{D}$ and A_{WP} are the mean draft and the waterplane area of the glacial ice at SWL. Notably, with changing vertical motion η_3 of the glacial ice, Eq. (39) takes into account the nonlinearities due to waterplane area change and the scenario when the entire glacial ice is fully submerged.

$$F_3^R = \rho g (\int D(s) ds - \eta_3) - Mg \tag{39}$$

Solving Eqs. (34) to (39) with an appropriate numerical scheme for ordinary differential equations (e.g., an explicit numerical scheme) yields the oscillatory motion of the glacial ice. In addition, an incomplete portion of the wave-driven drift motion is included in the model and should be filtered away from the results. Thereafter, the wave-driven oscillatory motion η_i (in the sway η_2 and heave η_3 directions) is constructed.

With known mean drift motion $V_i \times \mathrm{time}$ and the oscillatory motion $\eta_i(\mathrm{time})$ of the glacial ice feature, the glacial ice feature's motion can be written as $V_i \times \mathrm{time} + \eta_i(\mathrm{time})$ by superposition. Given the trajectory of the glacial ice feature, impact events (with information of vertical distribution of impact velocity) can be sampled (Lu and Amdahl, 2019, Fylling, 1994).

Annex B .4.2.3 The size effect of glacial ice features on the impact velocity

Depending on the relative glacial ice features' size/mass and wave conditions, the impact range and impact velocity will be different. Given the same wave condition, smaller glacial ice features experience a much more profound wave-driven oscillatory motion leading to a much wider impact range; whereas larger glacial ice features experience a more 'linear drifting pattern' motion leading to a more concentrated impact location. In addition, a larger impact velocity is normally expected for smaller glacial ice features. As the kinetic energy scales quadratically with the impact velocity, it is important to evaluate the potential impact damage caused by small glacial ice features.

Annex B .4.2.4 Influence of wave conditions on the impact velocity

Wave conditions can be characterised by different return periods and the associated $H_S - T_P$ combinations. Reasonable choices of these wave condition parameters shall be utilised to calculate the corresponding V_{impact} and thereby E_k^V distributions. For a given glacial ice feature, the general trend is that higher significant wave height H_S leads to larger impact velocities and wider range of impact locations. With respect to the choice on reasonable wave conditions given in different standards (NORSOK-N003, 2007, ISO19906, 2019) it is referred to the discussion in Commentary section Annex B .8.2.2.

Annex B .5 Damage assessment

Damage assessment may be carried out in a fully coupled, partially coupled, or decoupled manner. A description of the coupling strategies of different methods are summarised in Commentary section Annex B .8.3.

Annex B .5.1 Fully-coupled analyses

In fully coupled analyses, major interaction effects in a glacial ice impact event shall be considered including hydrodynamic forces, ice material modelling and structural resistance with proper fracture modelling. The modelling of the ice and the structure shall comply with the requirements in Annex B .5.5.2. The rigid body motion as given by the global geometries of the ice and the structure shall take into account relevant added masses. Constant added mass may be assumed. If the fluid is modelled as well (adopting e.g. the ALE), the correctness of the modelling shall be demonstrated for known solutions.

Annex B .5.2 Partially-coupled analyses

In the partially-coupled analyses, major interaction effects as required in fully coupled analyses shall be included. Simplified expressions are, however, used for ice damage and structural deformation, partially accounting for the effects of ice structure interactions. Refer Commentary section Annex B .8.4 for more details on the method and its implementation.

Annex B .5.3 Decoupled analyses

In the decoupled analyses, the external and internal mechanics calculations are performed independently.

Annex B .5.4 External Mechanics

The impact energy to be dissipated as strain energy may - depending on the type of installation and the purpose of the analysis - be taken as:

- Compliant installations:

$$E_s = \frac{1}{2}(m_s + a_s)v_s^2 \frac{\left(1 - \frac{v_i}{v_s}\right)^2}{1 + \frac{m_s + a_s}{m_i + a_i}} \tag{40}$$

- Single Point Anchored Reservoir (SPAR) platforms:

$$E_s = \frac{1}{2}(m_s + a_s)v_s^2 \frac{\left(1 - \frac{v_i}{v_s}\right)^2}{1 + \frac{m_s + a_s}{m_i + a_i} + \frac{(m_s + a_s)z_i^2}{I_i}} \tag{41}$$

- Fixed installations:

$$E_s = \frac{1}{2}(m_s + a_s)v_s^2 \tag{42}$$

m_s	=	ice mass
a_s	=	ice added mass
v_s	=	impact velocity
m_i	=	mass of installation
a_i	=	added mass of installation
v_i	=	velocity of installation
J	=	mass moment of inertia of installation (including added mass) with respect to effective pivot point
I_i	=	mass moment of inertia of installation (including added mass) with center of gravity
z	=	distance from pivot point to point of contact
z_i	=	distance from centre of gravity to contact point

Eccentric impacts with respect to the centre of gravity of the ice yield smaller demands for strain energy dissipation. This may be taken into account, provided that centric impact is not possible.

In most cases the velocity of the installation can be disregarded, i.e. $v_i = 0$.

In the general case, considering impact normal to a defined impact plane, the dissipated energy will have contributions from the relative motions tangential to- and normal to the impact plane. Disregarding the energy dissipated tangentially ("friction" energy), the energy dissipated in normal direction may be obtained as follows

$$E_s = \frac{1}{2}\bar{m}_s \bar{v}_s^2 \frac{\left(1-\frac{\bar{v}_i}{\bar{v}_s}\right)^2}{1+\frac{\bar{m}_s}{\bar{m}_i}} \tag{43}$$

where $\bar{v}_s$ and $\bar{v}_i$ are the velocity of ice and installation, respectively, taken normal to the impact plane (the signs are equal when moving in the same direction). The equivalent mass, $\bar{m}_j$, for the installation and ice, respectively, depends on the mass, $\bar{m}_{jx}, \bar{m}_{jy}, \bar{m}_{jz}$, and mass moment of inertia, $\bar{I}_{jx}, \bar{I}_{jy}, \bar{I}_{jz}$, about the three axes of the coordinate system including hydrodynamic added mass, all projected on the collision plane and is given by Popov et. al. (1967):

$$\bar{m}_j = \left(\frac{l_j^2}{\bar{m}_{jx}} + \frac{m_j^2}{\bar{m}_{jy}} + \frac{n_j^2}{\bar{m}_{jz}} + \frac{\lambda_j^2}{\bar{I}_{jx}} + \frac{\mu_j^2}{\bar{I}_{jy}} + \frac{\nu_j^2}{\bar{I}_{jz}}\right)^{-1}, \qquad j = s \text{ (ice)}, = i \text{ (installation)} \tag{44}$$

The collision point is described by the three coordinates (*x,y,z*) relative to the centre of gravity for the installation and the ice. *l,m,n* are the direction cosines for the unit vector normal to the collision plane (pointing outwards) where the location of the contact point is expressed in the two coordinate systems

$$P\left(x_j, y_j, z_j\right), \quad \mathbf{I}_j = l_j\mathbf{i} + m_j\mathbf{j} + n_j\mathbf{k} \qquad j = s \text{ (ice)}, = i \text{ (installation)} \tag{45}$$

The lever arms for roll, pitch and yaw motions are given by

$$\begin{aligned} \lambda_j &= mz_j - ny_j \qquad j = s \text{ (ice)}, = i \text{ (installation)} \\ \mu_j &= nx_j - lz_j \\ \nu_j &= ly_j - mx_j \end{aligned} \tag{46}$$

The calculation of the above parameters shall be performed for both the ice and the installation using a uniquely defined impact plane. The orientation of the collision plane is not always obvious. Normally, the stronger of the ice and the installation, or the object with a flat surface or a convex outer shape at the impact point shall be used as the master object to establish the local coordinate system (especially the normal direction). The averaged normal direction can be used when it is difficult to choose direction.

The tangential motion components on the collision plane related to ‘friction’ energy dissipation may also be taken into account using the complete 3D model developed by Liu and Amdahl (2019). This method considers two outcomes of the collision event, depending on the amount of friction forces along the collision plane, namely i) slide, where the two bodies move tangential to the collision plane, ii) stick, where the two bodies stick together. The sliding case with friction set to zero condensates into the solution given by Popov et. al. (1967).

The friction factor should take into account ice-to-steel friction as well as any transverse force due to deformation in the tangential direction. This force component is generally smaller than the force caused by pure lateral indentation, see Annex B .5.5.3.

For vertical impacts in downward direction it is normally conservative to assume that the entire kinetic energy has to be dissipated as strain energy in the installation. If the relative motion of the ice and installation is such that the installation tend to lift the ice out-of-water, it shall be verified that the installation is capable of producing this force level (normally with increased plastic deformations).

The installation can be assumed compliant if the duration of impact is small compared to the fundamental period of vibration of the installation. If the duration of impact is comparatively long, the installation can be assumed fixed.

Floating platforms (semi-submersibles, TLP's, production vessels) can normally be considered as compliant. Jack-ups may be classified as fixed or compliant. Jacket structures can normally be considered as fixed.

Annex B .5.5 Internal Mechanics

It is convenient to consider the strain energy dissipation in the installation on three different levels:

- local cross-section
- component/sub-structure
- total system

Interaction between the three levels of energy dissipation shall be considered.

Plastic modes of energy dissipation shall be considered for cross-sections and components /substructures in direct contact with the ice. Elastic strain energy can in most cases be disregarded, but elastic axial flexibility may have a substantial effect on the load-deformation relationships for components/sub-structures. Elastic energy may contribute significantly on a global level.

Often the integrity of the installation can be verified by means of simple calculation models described in Annex B .6.

Annex B .5.5.1 Ice-structure interaction

The relative strength of the glacial ice feature and the installation at the location of the contact determines which of the two bodies dissipates more impact energy at a given time. The softer of the two bodies dissipates more energy in forms of structural and/or ice deformation. The strength of the installation can formally be represented by the contact force – structural deformation relationship illustrated on the right-hand side of Figure 8; the strength of the glacial ice feature can be represented by the contact force –ice deformation relationship illustrated on the left-hand side of Figure 8. The part of the energy dissipated by the ice and the installation equals the total area under the two "contact force – deformation" curves.

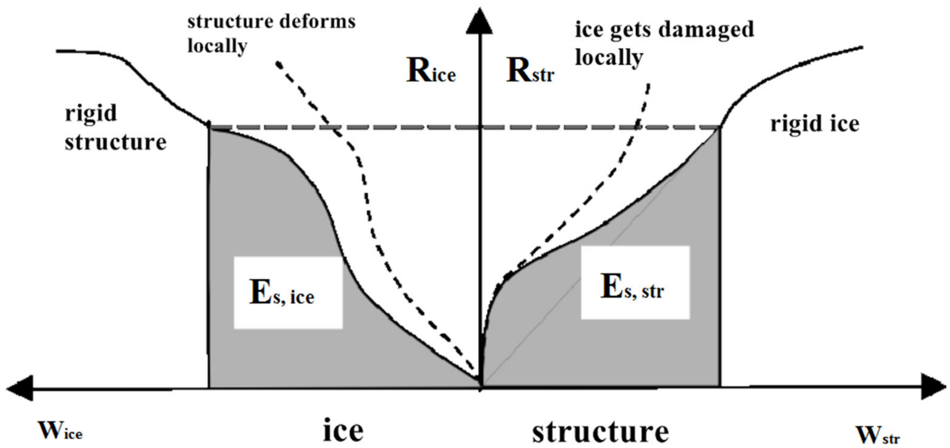

Figure 8. Energy dissipation in ice and installation.

As the load level is not known a priori an incremental procedure is generally needed.

$$E_s = E_{s,ice} + E_{s,str} = \beta \int_0^{w_{\text{ice,max}}} R_{ice} dw_{ice} + \int_0^{w_{\text{str,max}}} R_{str} dw_{str} \quad (47)$$

The contact force – deformation/crushing depth relationships for the ice and the installation are often established independently of each other assuming the other object infinitely rigid (presented by the solid dark curves in Figure 8). This method may have, however, severe limitations; i.e. both ice and the structure will dissipate some energy regardless of the relative strength.

Often the stronger of the ice and the installation will experience less damage and the softer more damage than what is predicted with the approach described above. As the softer structure/ice deforms, the impact force is distributed over a larger contact area. Accordingly, the resistance of the strong ice/structure increases. This will cause an "upward" shift of the resistance curve for the stronger ice/structure (refer to Figure 8). This coupling between the 'ice deformation process' and the 'structural deformation process' can be considered fully by the nonlinear analysis in Annex B .5.5.2 and partially by the analysis in Annex B .5.2.

Care should be exercised that the contact force – deformation curves calculated are a realistic representation of the interactive nature of the deformations taking place between ice and the structures.

The energy absorption capacity of the ice should be verified against target force-area curves for crushing against a rigid plane structure.

In lieu of more accurate analysis, the interaction effect may be taken into account by an energy dissipation correction factor β.

$$\beta = \frac{F_c - 1}{9}, \qquad \text{Max}\,1.0;\ \text{Min}\,0.0 \quad (48)$$

for glacial ice impacts against offshore structures, where F_c (unit: MN) is the initial collapse load of the structure. Refer to Commentary section Annex B .8.5 for the idea behind the correction factor.

Annex B .5.5.2 Nonlinear finite element analysis of ice and structures

Analysis of structural deformations by means of non-linear finite element methods shall follow the principles described in DNV-GL RP-C208 *Determination of Structural Capacity by Nonlinear FE analysis methods* (DNV-RP-C208, 2016). The fracture criterion for shell finite elements may be adopted. Crack propagation may be simulated by element erosion. The fracture criterion in DNV-GL RP-C208 is conservative, refer Commentary section Annex B .8.6, and other criteria may be adopted if verified against a sufficient number of representative tests, more detailed calculations or benchmark studies.

Modelling of the ice should be based on volume elements. The element size in the region of interest, i.e. in and close to the contact areas where ice deformation may take place, should as far as possible be uniform and of approximately the same dimensions as those representing the structure.

Ice under external loads may fail in different failure modes. Ice crushing with possible spalling shall be modelled in a glacial ice impact event. The behaviour of the ice during severe deformations may be based on plastic flow theory where the capacity is represented by a plastic potential, a crushable foam or other available ice models. The adopted ice model shall capture major macroscopic characteristics of glacial ice, e.g. ice confinement under hydrostatic pressure. Extensive deformation of ice may be taken into account by element erosion, smooth particle hydrodynamics, cohesive elements or equivalent methods.

The adopted ice model shall be calibrated by deforming it against a *plane rigid wall* such that the desired force-area relationship is obtained over the deformation range of interest. As the simulated ice deformation behaviour depends on the element size, calibration shall be valid for the element size that is actually used in the ice-structure interaction analysis.

If substantiated by experiments, the ice may be calibrated by simulating penetration of a rigid body into an ice block. It has to be demonstrated that the confinement effect is correctly represented in the material model by also simulating ice deformation against a plane wall. Refer Commentary section Annex B .8.7 for an example on the calibration of an ice material model.

The material model used for the ice feature shall be calibrated against a selected force-area relationship. The average pressure shall be relatively insensitive to the size of the contact area. Unless proved to be more relevant, the following force-area curve shall be adopted:

$$F = C_0 A^{0.9} \tag{49}$$

In lieu of test data, C_0 = 3.2 may be used for the Barents Sea. Refer to Annex B .8.8 for more details on the recommended force area curve.

Annex B .5.5.3 Oblique impact with moving ice load

Moving ice load denotes the action that is generated when the ice slides along the structure. For a given indentation, the structural resistance to a moving load will often be smaller than that caused by penetration normal to the panel, refer Commentary section Annex B .8.9.

Fully coupled analyses shall be performed in accordance with Annex B .5.1 to simulate realistic rigid body motions of ice and the structure, such that combined actions of ice indentation and sliding can be properly accounted for.

In lieu of more accurate simulations, analysis of structural response to moving loads may be carried out with prescribed ice motions by first producing an initial indentation depth and then move the ice along the structure with constant indentation. Simulations shall be carried out with different initial indentation depths, so as to allow interpolation of the moving ice loads when the indentation varies during the contact.

Annex B .6 Force-deformation relationships for beams and stiffened plates

Annex B .6.1 General

The response of a beam, viz. a stiffener with associated plate flange, subjected to ice load is initially governed by bending, which is affected by and interacts with local deformation of stiffener webs under the load. The bending capacity is also reduced if local buckling takes place on the compression side. As the beam undergoes finite deformations, the load carrying capacity may increase considerably due to the development of membrane tension forces. This depends upon the ability of adjacent structure to restrain the connections at the member ends to inward displacements. Provided that the connections do not fail, the energy dissipation capacity is either limited by tension failure of the member or rupture of the connection.

Simple plastic methods of analysis are generally applicable. Special considerations shall be given to the effect of:

- elastic flexibility of member/adjacent structure,
- local deformation of cross-section,
- local buckling,
- strength of connections,
- strength of adjacent structure, and
- fracture.

Annex B .6.2 Plastic force-deformation relationships of beams with axial flexibility

Relatively small axial displacements have a significant influence on the development of tensile forces in members undergoing large lateral deformations. Equivalent elastic, axial stiffness k_{eq} may be defined as:

$$\frac{1}{k_{eq}}=\frac{1}{k_{\text{node1}}}+\frac{1}{k_{\text{node2}}}+\frac{L}{EA} \tag{50}$$

k_{node1}, k_{node2}= axial stiffness of the nodes at each end of the beam with the considered member removed. This may be determined by introducing unit load in member axis direction at the end nodes with the member removed.

Plastic force-deformation relationship for a beam differs with cross sections, resulting from the fact that each beam cross section yields a plastic interaction function between axial force and bending moment. The section concerns mainly a beam with the stiffened-panel type cross section used widely in ships and offshore structures, where the area of plate flange is typically larger than the area of stiffener cross section. Plastic force-deformation relationships for other beam types are given in DNV-RP-C204 (2019).

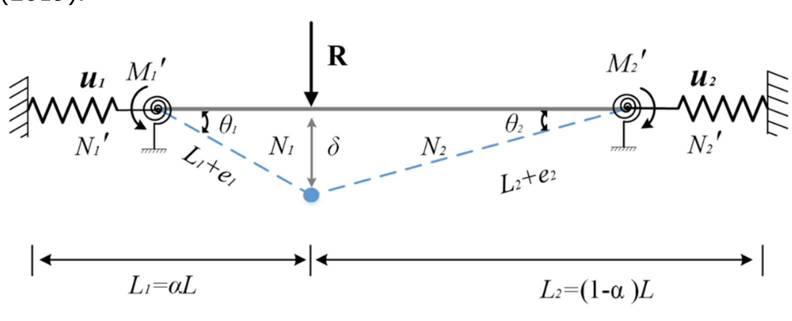

Figure 9. plastic deflection of a beam subjected to lateral loads with finite axial stiffness.

The formulation for the structural resistance of a beam , viz. a stiffener with associated plate flange, undergoing finite deformations is based on the work by Yu et al. (2018). The resistance R is given by the following equations:

$$\frac{R}{R_0}=\frac{M}{M_p}+\frac{N\delta}{\beta M_p}; \quad \beta=\begin{cases}1 & \text{free rotation}\\ 2 & \text{fixed rotation}\end{cases} \tag{51}$$

where the resistance to plastic bending collapse, R_0, fully plastic bending moment, M_p, and fully plastic axial force, N_p, of the stiffener with associated plate flange are given by:

$$\begin{aligned} R_0 &= \beta M_p\left(\frac{1}{\alpha L}+\frac{1}{(1-\alpha)L}\right)\\ M_p &= \sigma_y\left(\frac{1}{2}A_w h_w + A_t h_w\right)\\ N_p &= \sigma_y A_e \end{aligned} \tag{52}$$

The development of the membrane force N is determined by:

$$\begin{aligned} \frac{N}{N_p} &= \left(\frac{16}{\beta^2 c}\left(\frac{A_w}{A_e}\right)^2-\left(2\frac{A_p}{A_e}-1\right)\right)\left[\exp\left(-\frac{\beta c}{4}\frac{A_e}{A_w}\frac{\delta}{h_w}\right)-1\right]\\ &\quad +\frac{4}{\beta}\frac{A_w}{A_e}\frac{\delta}{h_w}; \quad \left(\text{stage 1, 2, 3}: \frac{N}{N_p}<1\right)\\ \frac{N}{N_p} &= 1; \quad \text{stage 4} \end{aligned} \tag{53}$$

where ***c*** is the non-dimensional axial stiffness given by:

$$c=\frac{k_{eq}h_w^{\ 2}}{\alpha(1-\alpha)LN_p} \tag{54}$$

The development of the bending moment M is calculated from:

$$\begin{aligned} \frac{M}{M_p} &= 1; \quad \left(\text{stage 1}: \frac{N}{N_p}\le\frac{2A_p}{A_e}-1\right)\\ \frac{M}{M_p} &= 1-\frac{1}{4}\frac{1}{1+2\frac{A_t}{A_w}}\left(\frac{A_e}{A_w}\right)^2\left(\frac{N}{N_p}-\left(\frac{2A_p}{A_e}-1\right)\right)^2; \quad \left(\text{stage 2}: \frac{2A_p}{A_e}-1<\frac{N}{N_p}<1-\frac{2A_t}{A_e}\right)\\ \frac{M}{M_p} &= \frac{\frac{A_e}{A_w}}{1+2\frac{A_t}{A_w}}\left(1-\frac{N}{N_p}\right); \quad \left(\text{stage 3}: 1-\frac{2A_t}{A_e}\le\frac{N}{N_p}<1\right)\\ M &= 0; \quad \text{stage 4} \end{aligned} \tag{55}$$

L	= member length
σ_y	= yield stress of the member material
A_t	= area of the stiffener top flange

A_w	= area of the stiffener web
$A_s = A_w + A_t$	= area of the stiffener including stiffened web and flange
A_p	= area of the plate flange
$A_e = A_p + A_w + A_t$	= total area of stiffener and plate flange
h_w	= web height of the stiffener
δ	= deflection of the beam
s	= width of the stiffened panel
b	= length of the loading patch

The resistance of the stiffened plate depends upon the non-dimensional axial flexibility c(k), the relative size of the plate flange vs stiffener area ($A_p / A_s \geq 1$) and the size of the top flange versus the web area (A_f / A_w), as shown in Figure 10 and Figure 11.

Note that the plastic interaction relationships are based upon compact cross-section behaviour through sustained plastic deformations. Webs of stiffeners shall comply with $h_w/t_w < 20$. The accuracy of the equations may decrease due to shear effects when $L/h_w<10$.

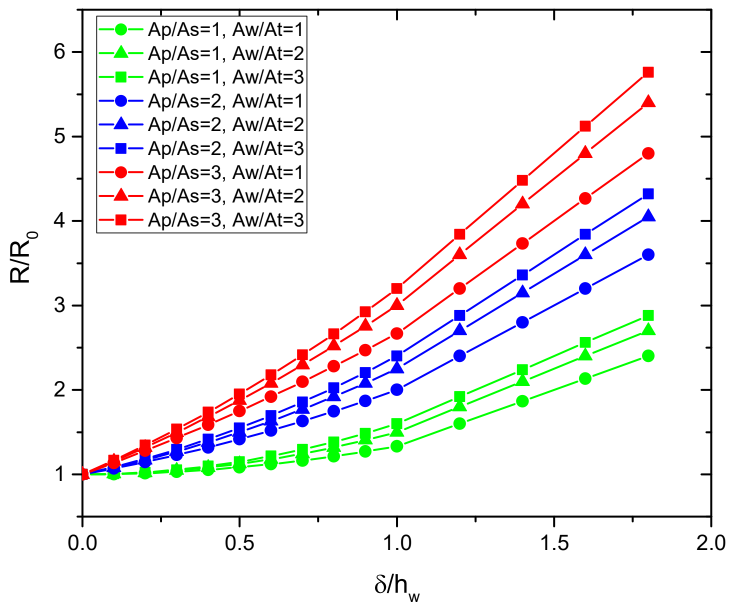

Figure 10. Plastic load-deformation relationship for stiffened plates with fixed ends (the plate flange is larger than stiffener area).

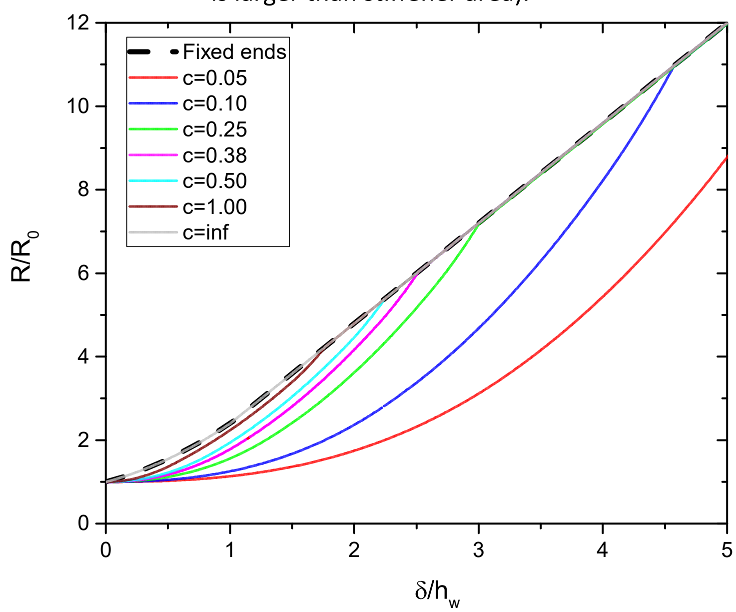

Figure 11. Plastic load-deformation relationship for stiffened plates with different axial stiffness.

For a stiffened plate under pressure patch loading, the resistance, r_b [Pa], is expressed by,

$$r_b = \frac{R}{bs\left(1-\frac{b}{2L}\right)} \tag{56}$$

s is the width of the plate flange and b is the length of the patch load.

Annex B .6.3 Plastic force-deformation relationships of stiffened panels

For stiffened panels with several bays undergoing large deflections, the resistance shall include two main components:

- beam deformation mode of the various stiffened plates as given in Annex B .6.2;
- membrane forces in the transverse direction.

The shell plating of a stiffened panel will be subjected to biaxial tension when it undergoes large indentation due to ice action. According to von-Mises yield criterion, the tensile stresses may reach the yield stress level in the two orthogonal directions. Hence, the two contributions can be treated independently.

For a stiffened panel subjected to patch or uniform loading (refer Figure 12), the displacement of the shell plating is assumed to have a sinusoidal shape in transverse direction and linear in the longitudinal direction.

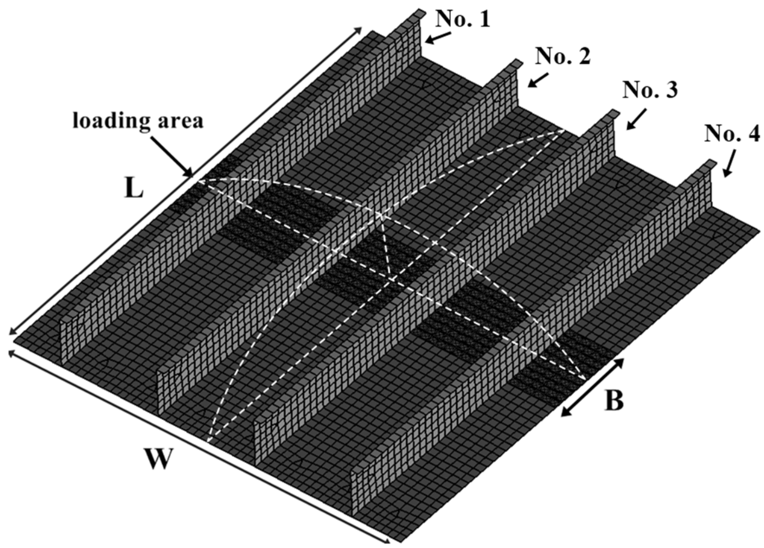

Figure 12. Deformation of a stiffened panel consisting of 4 bays subjected to pressure patch loading. The dashed lines denote deflections of the panel.

The resistance $r_{b,i}$ [Pa] for the i_{th} beam (stiffener with associated plate flange) of a stiffened panel shall comply with formulations in Annex B .6.2, where the deflection of each beam decreases sinusoidally from panel middle to the boundary.

The resistance, r_m [Pa] due to membrane stretching of the shell plating in transverse direction is given by,

$$r_m = \frac{\pi^4 N_0 \delta}{16W^2 \sin\left(\frac{B\pi}{2L}\right)} \tag{57}$$

Where, *L* is the panel length, W is the panel width, *B* is the length of the patch load in stiffener direction, δ is the panel central deflection, $N_0 = \sigma_y t_p$ is the fully plastic tension force per unit length, t_p is the thickness of the bottom plate.

When $B = L$, i.e. the pressure is uniformly distributed over the whole panel, the pressure is:

$$\text{if } B \to L, \quad \text{then } r_m \to \frac{\pi^4 N_0 \delta}{16W^2} \tag{58}$$

The resultant pressure loading thus yields $r = \sum_i r_{b,i} + r_m$.

Annex B .6.4 Plastic force-deformation relationships of web girders

When the adjacent frames/stringers of a stiffened panel cannot support the panel resistance in the web plate direction, or is subjected to direct contact with the ice, the web plates may deform. Additional energy will be dissipated by the folding type deformation of the frames/stringers web plates, but the resistance of the stiffened panel as a function of lateral deformation will be delayed accordingly. The in-plane crushing resistance of web girders may be taken into account using methods by Hong and Amdahl (2008). The resistance of the first fold reads,

$$R(\delta) = \frac{1.2 M_0 a}{H\sqrt{1-\left(1-0.3\dfrac{\delta}{H}\right)^2}} \left(2 + \frac{\left(1-0.3\dfrac{\delta}{H}\right)}{\sqrt{3+\left(1-0.3\dfrac{\delta}{H}\right)^2}} \right) + 5.56\frac{N_0 H \delta}{a} \tag{59}$$

where, t_w is the thickness of the web girder, δ is the crushing displacement of the web girder, a is half span of the web girder, $M_0 = \frac{1}{4}\sigma_0 t_w^2$ is fully plastic bending moment per unit length, $N_0 = \sigma_0 t_w$ is the fully plastic tension force per unit length, $\sigma_0 = \left(\sigma_y + \sigma_u\right)/2$ is the flow stress. $H = 0.395 a^{2/3} t_w^{\ 1/3}$ is the characteristic crushing depth of the web girder.

The mean crushing resistance of the web girder yields,

$$\frac{P_m}{M_0} = \frac{17.0}{\lambda}\left(\frac{a}{t_w}\right)^{1/3} \tag{60}$$

The formulation is derived for the crushing resistance of web plates and applies to web girders equipped with horizontal stiffeners, where the influence of horizontal stiffeners is limited.

Annex B .7 Global Integrity during Impact

Normally, it is unlikely that the installation will turn into a global collapse mechanism under direct impact load, because the impact load is typically an order of magnitude smaller than the resultant design wave force.

Linear analysis often suffices to check that global integrity is maintained. The installation should be checked for the maximum impact force.

For installations responding predominantly statically, the maximum impact force occurs at maximum deformation. For structures responding predominantly impulsively, the maximum impact force occurs at small global deformation of the platform. An upper bound to the impact force is to assume that the installation is fixed with respect to global displacement.

Annex B .8 Commentary Section

Annex B .8.1 Critical local ice geometry

This section gives additional comments to Annex B .3 in relation to the critical local ice geometry. Figure 13 demonstrates the importance of the local ice geometry on the penetration into the column of a semi-submersible platform. The force for rigid ice/deformable structure and deformable ice/rigid structure are plotted in black while the results from NLFEM considering fully ice structure interactions are plotted in red. When the radius of curvature is small (i.e., a sharp ice body), the ice crushes substantially and the column is subjected to small deformations. As the radius of curvature increases (i.e., the ice gets blunter), the structure starts to deform more, and the ice becomes more confined and consequently stronger. At a certain radius (curvature radius/panel length=0.81) the ice is subjected to little deformation and the response of the column is virtually identical to that under the impact of a rigid ice feature. When the ice becomes even blunter, the ice still behaves as if it is rigid and the column dissipates most/all the impact energy with, however, less structural deformation as the contact area / deformation area is relatively large.

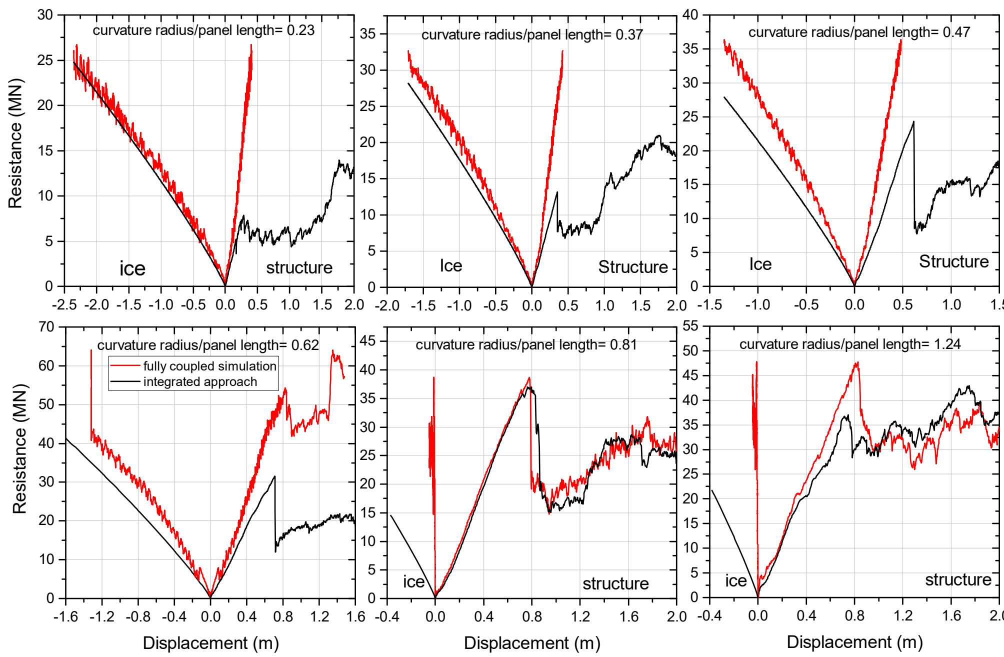

Figure 13. Force deformation curves of ice and the structure when ice with different curvature radius impacts stiffened panels of a semi-submersible platform.

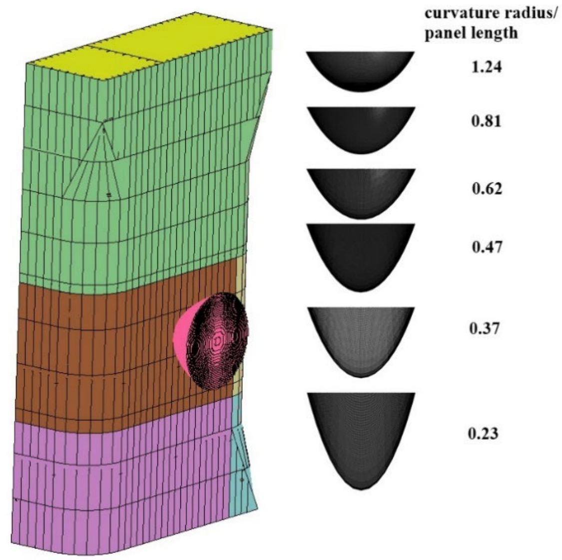

Figure 14. The effect of local geometry on penetration into the platform.

Annex B .8.2 Ice impact velocity and kinetic energy

This section gives additional comments to Annex B .4 in relation to the ice impact velocity and kinetic energy. The ice impact velocity depends on the following parameters, whose major dependent parameters are also listed:

- Mass/size of the glacial ice features (site dependent)
- Mean drift velocities (depends on the mass/size and considered wind, wave and current conditions at the site)
- Wind, wave and current conditions (depends on the return period and possible $H_S - T_P$ combinations)

When the glacial ice conditions have been quantified, the mass/size distribution *M* and its associated mean drift velocity V_i should be established for the considered wave conditions. The next step is to calculate the oscillatory motion and extract the impact velocity distribution (see the procedures and formulations described in Annex B .4). Ideally, this should be repeated for various mass/sizes of the glacial ice features and various wave conditions. However, this is computationally expensive. Potential simplifications are described in the following:

Annex B .8.2.1 Simplification in mass/size considerations

The wave-driven oscillatory motion is normally prominent only for small glacial ice features. For large glacial ice features, the drift motion (driven by wind, wave and current) is dominant. Thus, for large icebergs only the mean drift velocity V_i needs to be accounted for, and the formulation in Eq. (6) can be simplified into Eq. (61).

$$E_k^V = \frac{1}{2}(M + A)(V_i)^2 \quad \text{for } L_i > L_{cr} \tag{61}$$

For small to medium sized glacial ice features, the 'simple nonlinear model' introduced in Annex B .4.2 based on long wave assumption will normally suffice. However, further studies are required to establish the length limit, L_{cr} , beyond which Eq. (61) can be applied.

Another possible simplification is to decouple the dependence between the mean drift velocity V_i and the mass distribution M. Further studies are needed to confirm the validity of this approach.

Annex B .8.2.2 Wave condition considerations

The kinetic energy of glacial ice features depends upon the wave conditions. At a specific site, wave conditions are associated with different return periods. For a given return period, there are different $H_S - T_P$ combinations. The choice of return periods should be considered together with the encounter frequency of glacial ice features and the target design level; the choice on the $H_S - T_P$ combination should be based on sound engineering judgement. Regarding the choice of wave return periods used to calculate the kinetic energy of the glacial ice features, it is possible to follow recommendations stated in existing standards (e.g., (NORSOK-N003, 2007, ISO19906, 2019). Further discussions are is presented in Annex B .8.2.3). However, preliminary calculations of the design kinetic energy E_k^{design} indicate that both recommendations are too conservative. Further studies are needed, to come up with a better and/or more clear suggestion on this issue.

Annex B .8.2.3 Load combination according to ISO19906 and NORSOK N-003

When calculating the design kinetic energy E_k^{design} for the ALS condition, the accompanying environmental load effects, due to e.g. wave actions, should be considered. The approaches adopted by ISO19906 and NORSOK N-003 are different.

In NORSOK N-003 (see the following original table for ALS #6), the wind, wave and current conditions for one-year return period are chosen. The motion of glacial ice features can therefore be calculated based upon these environmental conditions. The accompanying environmental effects (with an annual exceedance probability of 0.63) are to be combined with the effects of ALS level glacial ice impact to evaluate the structural damage.

Table 7 – Combination of water levels, metocean and earthquake conditions with expected mean values and annual probability of exceedance 10^{-2} and 10^{-4}

Limit states		Wind	Waves (e	Current (f	Sea spray icing	Sea ice	Ice-bergs	Snow	Earth-quake	Sea level (a
Ultimate limit states	1	10^{-2}	10^{-2}	10^{-1}	-	-	-	-	-	$HAT + S_{10^{-2}}$
	2	10^{-1}	10^{-1}	10^{-2}	-	-	-	-	-	$HAT + S_{10^{-2}}$
	3	10^{-1}	10^{-1}	10^{-1}	10^{-2}	-	-	10^{-1}	-	MWL
	4	10^{-1}	0,63 (c	10^{-1}	-	10^{-2}	-	-	-	MWL
	5	10^{-1}	10^{-1}	10^{-1}	-	-	10^{-2}	-	-	MWL
	6	10^{-1}	10^{-1}	10^{-1}	10^{-1}	-	-	10^{-2}	-	MWL
	7	-	-	-	-	-	-	-	10^{-2}	MWL (b
Accidental limit states	1	10^{-4}	10^{-2}	10^{-1}	-	-	-	-	-	$MWL + S_{10^{-4}}$
	2	10^{-2}	10^{-4}	10^{-1}	-	-	-	-	-	$MWL + S_{10^{-4}}$
	3	10^{-1}	10^{-1}	10^{-4}	-	-	-	-	-	$MWL + S_{10^{-4}}$
	4	10^{-2}	10^{-1}	-	10^{-4}	-	-	-	-	MWL
	5	-	-	-	-	10^{-4} (d	-	-	-	MWL
	6	0,63	0,63	0,63	-	-	10^{-4} (d	-	-	MWL
	7	0,63 (g	0,63 (g	-	-	-	-	10^{-4}	-	MWL
	8		-		-	-	-	-	10^{-4}	MWL (b

a) HAT: Highest Astronomical Tide; MWL: Mean water level; MWL+S: Mean water level, including the effect of storm surge with given q-probability

b) Seismic response analysis should be carried out for the most critical water level.

c) In determination of the combination of sea ice and other action contributions, the exposure period should be evaluated in order to establish associated values of wind, waves and current.

d) With respect to ULS and ALS related sea ice and iceberg actions, it shall be acknowledge that there are several realisations of the ice/iceberg conditions that can cause actions corresponding to these exceedance levels. Further, it shall also be acknowledge that the ice conditions also will depend on the failure mode under consideration

e) If using the contour line approach, the worst combination of Hs/Tp for the given q-probability shall be used.

f) For current a 1-hour mean shall be used for 10^{-1} values and 10 min mean for 10^{-2} and 10_{-4} values, as described in 6.2.2.2

g) If effects of wind drift not are included in ALS estimate for snow actions, action contributions from wind and waves can be excluded

In ISO19906 (see the following original tables for AL actions), the accompanying environmental actions are chosen corresponding to the EL design (i.e., with annual exceedance probability of 10^{-2}), however, with a load reduction factor of 0.4 or 0.5.

The difference and validity of these procedures should be evaluated in future work.

In addition, as the motion of small glacial ice features is stochastically dependent upon the wave conditions, a wave condition with a reasonable return period should be chosen taking into account the encounter frequency. For example, with an encounter frequency of 10^{-3}, it is no longer reasonable to choose a wave condition with a non-exceedance level of 10^{-2} (as it is now stated in ISO19906) to calculate the 10^{-4} design kinetic energy. An elucidation on this requires further studies.

Table 7-1 — Companion EL environmental actions

Principal action (EL or AL)	Companion EL environmental action		
	Stochastically dependent	Stochastically independent	Mutually exclusive
Isolated ice features (e.g. ice floes, ridge fragments, stamukhi, bergy bits, small icebergs)	Wind, wind-driven current, tidal and background current, waves[b]	Waves[b]	—

[a] For the AL earthquake, it is normally sufficient to consider only ice likely to be present when an earthquake occurs.
[b] The principal action from small icebergs or ice floes and the companion wave actions can be stochastically dependent.
[c] Categorisation of companion actions for snow and icing should be assessed for site-specific conditions.

Table 7-2 — Combination factors for companion EL environmental processes

Principal action	Factor for representative EL companion environmental action	
	Companion action is stochastically dependent on the principal action	Companion action is stochastically independent of the principal action
EL action	0,9	0,6
AL action	0,5	0,4

Annex B .8.3 Damage assessment

This section gives additional comments to Annex B .5. The methods for the damage assessment are classified into three main categories in Annex B .5 based on different coupling strategies, where the decoupled method can further be subdivided depending on the treatment of internal mechanics. Figure 15 summarises the methods and associated coupling strategies.

The fully coupled method includes major interaction effects, e.g., hydrodynamic forces, ice material modelling and structural simulation. It represents the most detailed analyses alternative and is suitable for performing damage assessment at selected critical locations, and for verification of simplified methods.

The partially coupled method accounts for the ice structure interaction in a simplified manner. An advantage of the method is that it is computationally efficient such that a large amount impact scenario at different structural locations can be carried out. This builds a complete picture of the structural damage information and exposes critical locations that experience maximum structural damage. This method should be verified against the fully coupled method or equivalent before massive simulations are performed (refer Commentary section Annex B .8.4).

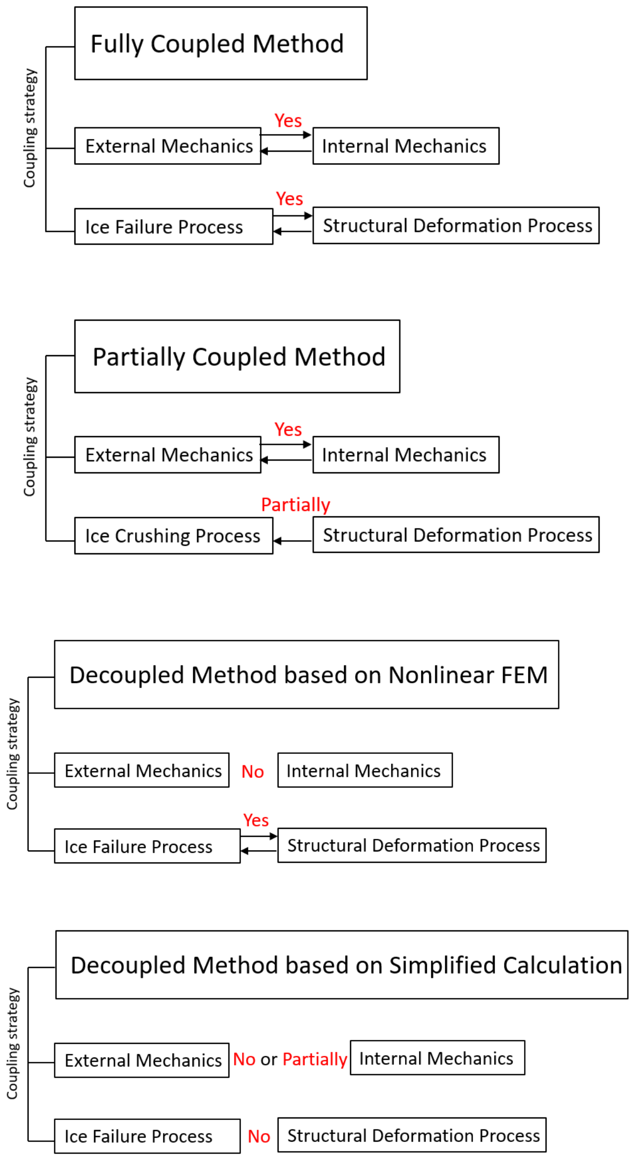

Figure 15. Analyses methods based on different coupling strategies.

The Nonlinear FEM – based decoupled approach focuses on the internal mechanics and shall yield realistic ice structure interactions for various ice local geometries. Refer Annex B .5.5.2 for more details.

The resistance to deformation and penetration can be based either on simplified formulas (see Annex B .6) or nonlinear finite element analysis of a rigid ice feature impacting a deformable structure.

Annex B .8.4 Partially-Coupled Analysis

This section gives additional comments to Annex B .5.2 concerning the partially-coupled analysis. When the local geometry of a glacial ice feature is not sharper than the critical sharpness (refer Annex B .3), ice crushing does not influence the structural deformation significantly. Thus, the partially-coupled method with one-way coupling (i.e., the ice crushing process is influenced by structural deformation but not vice versa) may be used with acceptable accuracy.

Figure 16 compares the maximum structure damage (in form of structural deformation) predicted with different methods for various local sharpness of the glacial ice feature (Lu et al., 2019). The partially-coupled analysis yields reasonably good results with significantly less computational costs when the radius of curvature of the local ice geometry is larger than 0.8 times of the stiffened panel length.

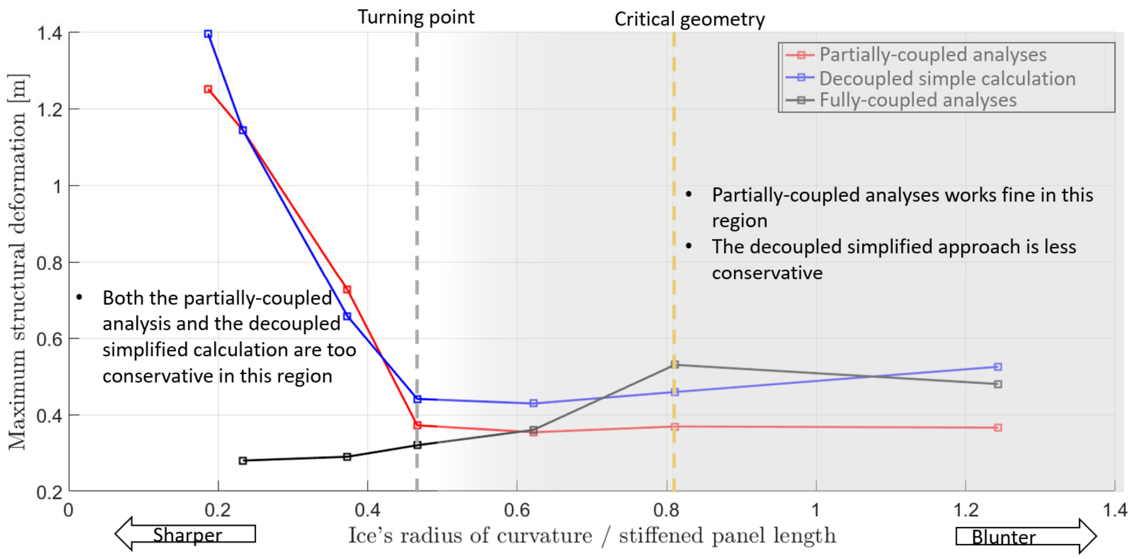

Figure 16. Application of different methods with varying local sharpness of the glacial ice feature.

While performing partially-coupled analyses, the customised ice - structure contact algorithm shall take into account ice deformation characterised as force versus nominal contact areas or force – deformation relationships at various locations of the installation. The force – displacement curves at various structural locations are inputs to the simulator and shall be obtained a prior through nonlinear dynamic finite element analysis. The number of curves should be sufficient to cover all the representative locations. Figure 17 shows an example of eleven representative impact locations that were investigated for a semi-submersible structure (Lu et al., 2018).

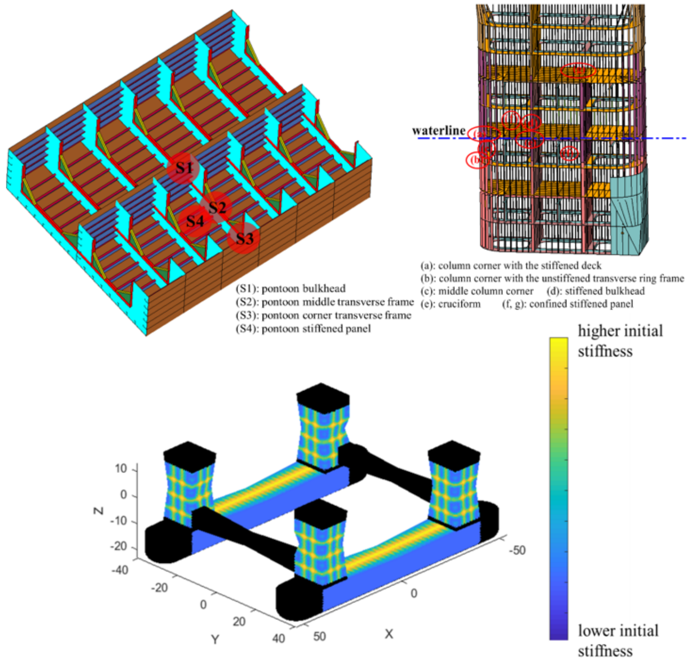

Figure 17. Construction of the local response curves around an installation (e.g., a semi-submersible) based on selected 11 representative locations on the pontoon and column (dark regions have no data).

To obtain comprehensive information of structural damage, at least 1000 impact scenarios (covering various impact heights, orientations and angles of the incoming glacial ice feature) should be simulated for one quarter of the structure (if the structure the quarterly symmetric). The massive simulation results can be summarised into a damage map with colours representing severity of structural damage, as exemplified in Figure 18.

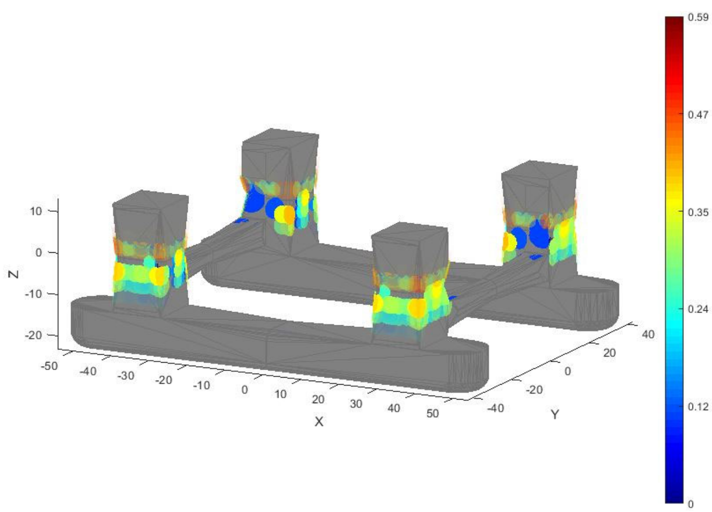

Figure 18. An example of damage map obtained by simulating around 1800 impact events at a quarter of the structure. A maximum deformation around 0.59 m and critical locations are illustrated.

Annex B .8.5 The Correction Factor

This section gives additional comments to Annex B .5.5 in relation to the correction factor. The correction factor given in Annex B .5.5 originates from observations of the damage obtained in coupled numerical simulation conducted by Yu et al. (2019). Figure 19 shows force deformation relationships for an ice feature with 2.3 m radius of curvature impacting different locations on a semi-submersible platform column. The dark curves in the 'structure domain' of the plots are obtained using the *ductile design* approach; the red curves are obtained by performing fully coupled ice-structure interaction analysis.

The effect of ice structure interaction is shown to be closely related to the initial collapse resistance of the studied strength members, which is about 1MN for stiffened panels, 4 MN for the platform bulkhead and 10 MN for the intersection of the bulkhead and the deck, respectively. This leads to ductile response for the stiffened panels (red and dark curves for structural deformation overlap with each other), shared energy response for the platform bulkhead and strength response for the intersection (red and dark curves for ice crushing process overlap with each other), considering a total energy of 7.5 MJ.

Therefore, a simple treatment is to relate the interaction effect to the initial collapse load of the structure. The strength design corresponds to a correction factor of 1.0 and ductile design 0.0. Linear interpolation is used between the two extremes.

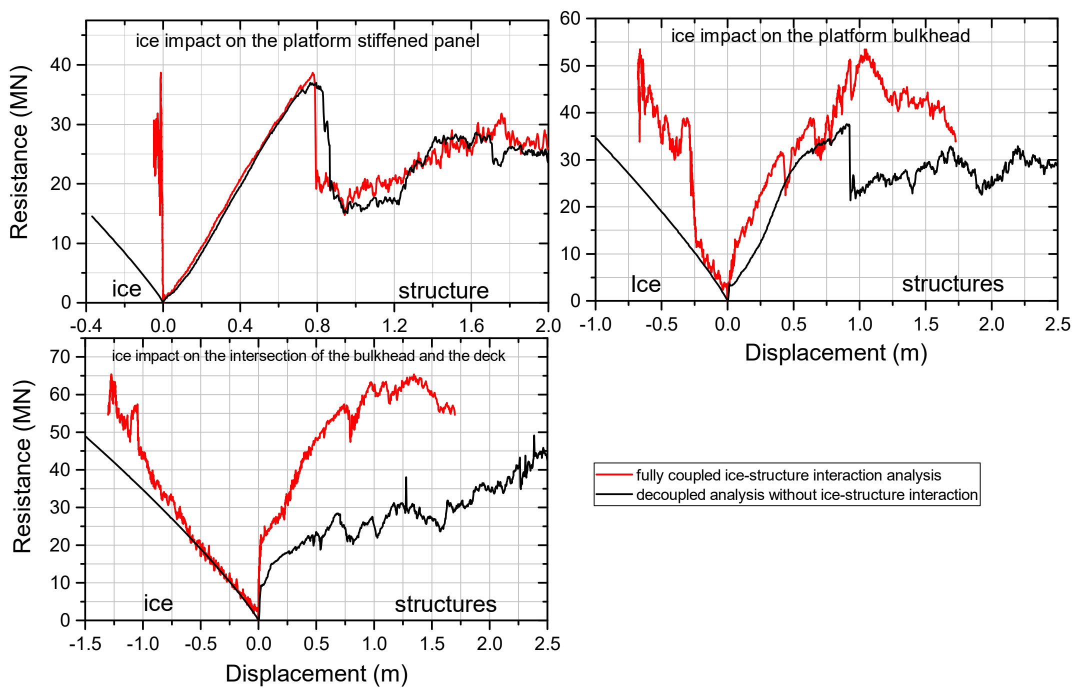

Figure 19 Force deformation relationships for a semi-submersible and ice with a curvature radius of 2.3 m.

Annex B .8.6 Discussion of the fracture criterion recommended in DNV RP C208

This section additionally discusses the fracture criterion recommended in DNV RP C208 in Annex B .5.5.2. Storheim et al. (2017) discussed the accuracy of different fracture criteria in Figure 20 and Figure 21 by comparing simulation curves with results from the stiffened panel indentation experiments by Alsos and Amdahl (2009) and the plate tearing tests by Simonsen and Törnqvist (2004).

The results show that the fracture criterion recommended by DNV RP C208 predicts too early fracture with the peak structural resistance being virtually half of the experimental capacity. This is considered overly conservative. The BWH criterion agrees reasonably well with the experimental curve.

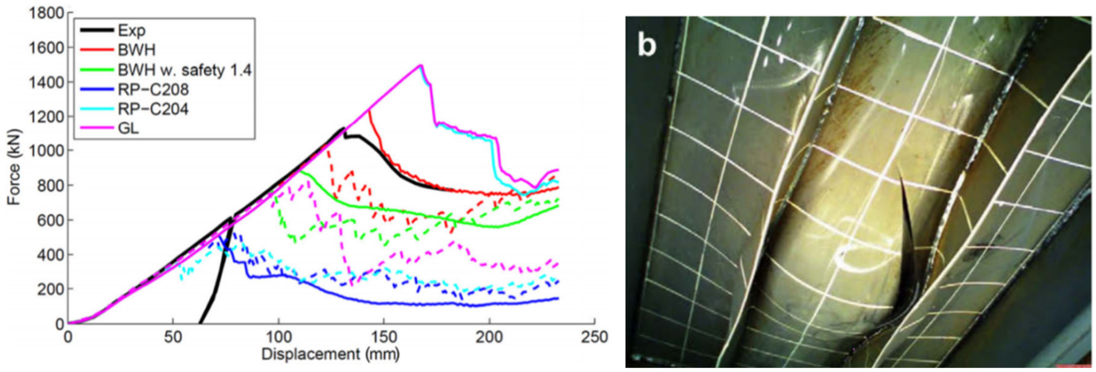

Figure 20. Force-displacement results from simulation of the indentation experiment two flatbar stiffeners from Alsos and Amdahl (2009) with different fracture criteria. Continuous lines are with element length equal to thickness, whereas dashed lines are with element length ten times the thickness. Data and simulation from Storheim et al. (2017).

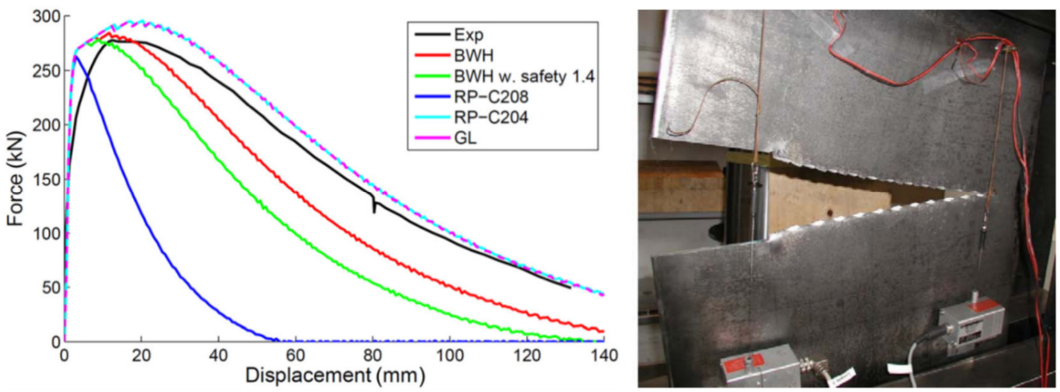

Figure 21 Force-displacement results from simulation of the plate tearing tests from Simonsen and Törnqvist (2004) using different fracture criterion with the element length equal to thickness. Data and simulation from Storheim et al. (2017).

Annex B .8.7 Calibration of ice material models

This section gives additional discription to Annex B .5.5.2 concerning the calibration of ice materials. The background for the requirement that the ice model used in the damage calculation must be calibrated against a target curve is demonstrated by the force-displacement curves in Figure 22. With a common failure criterion, the ice force-deformation curve increases with increasing volume element size. Thus, the failure criterion must be adjusted for different sizes so as to match the target design curve.

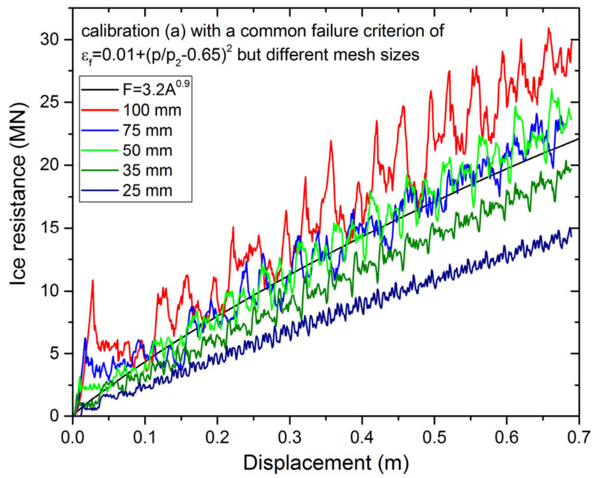

Figure 22. Mesh size dependence of ice crushing (the dark curve is the target force – displacement curve).

Figure 23 shows the results of two different numerical setups for calibration of the ice material to match the target force-deformation relationship (black curve). The red curve is obtained by pushing a spherical, rigid indenter into an ice block (Figure 24 left). Because the ice block has a relatively high confinement, material parameters representing relatively weaker ice (i.e., early failure strains) are needed to match with the dark curve. When a spherical ice with the same radius is crushed against a rigid wall using the above calibrated failure criterion, the lower blue curve is obtained due to less confinement.

However, if calibration is made by directly crushing a spherical ice feature with a rigid wall (Figure 24 right), material parameters corresponding to a stronger ice is needed due to less confinement (the green curve).

The behaviour for the blue curve (i.e., weak ice) seems physically sound, but experimental evidence is lacking at present. Hence the ice material should be conservatively calibrated against the target curve by crushing an ice indenter against a *rigid, plane plate* as shown by the green curve.

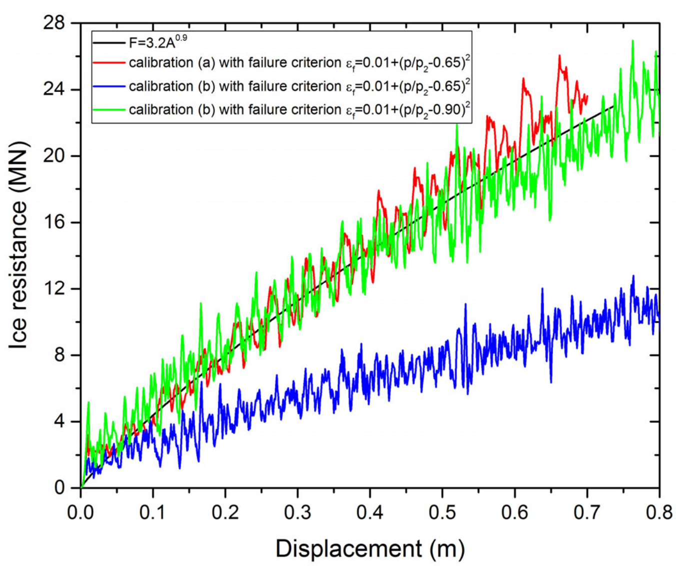

Figure 23. Ice force-deformation curves and corresponding failure criterions using two different ways of calibration.

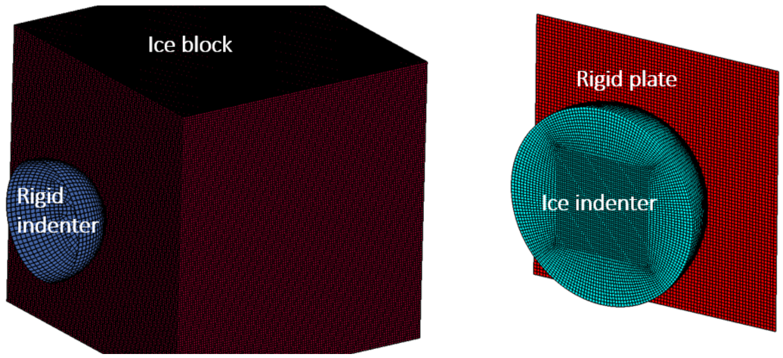

Figure 24. Two numerical setups to calibrate the ice material model (the right-hand side numerical set up is recommended).

Annex B .8.8 Pressure area relationship

This section presents some comments to the pressure area relationship in Annex B .5.5.2. Ice actions on offshore structures are often described via pressure-area (p-A) relationships of the form $p= C_0A^{ex}$ where C_0 is a constant. The exponent *ex* is typically in the range of -0.7 to 0.0 for local design of plates and stiffeners in the ULS (actions with annual probability of occurrence 10^{-2}). Thus, the pressure decreases fast with increasing area. The same expression, but with a larger C_0, is often specified for ALS conditions (annual probability of occurrence 10^{-4}). Unless strength design is aimed for, it is not necessary to check plates and stiffeners for these pressure levels. ALS checks concern generally deformations of stiffened panels and adjacent frames, decks etc., where the local high-pressure zones considered in ULS design are of less relevance. Thus, average pressures (process pressures) that are significantly less dependent on the contact area should be used. Unless otherwise substantiated by experiments, *ex* = -0.1 should be adopted. The factor C_0 depend on the ice conditions in the area. In lieu of more accurate information, for structures operating in the Barents Sea it is recommended to use C_0 = 3.2 adopted in the IACS UR for PC3 Polar class ships (IACS, 2011). This corresponds quite well to the average forces obtained in the Pond-Inlet tests with 2.3 m radius indenter (GEOTECH, 1985).

Annex B .8.9 Moving ice loads

Additional comments on moving ice load in Annex B .5.5.3 are presented here. The structural resistance to a moving ice load may be considerably smaller than that caused by lateral indentation to the same depth. Figure 25 shows the resistance of a stiffened panel in a semi-submersible platform column subjected to moving ice loads with different indentation depths. The force level during the sliding phase is virtually half of the peak value of the indentation stage provided that the outer shell is not torn open (dent depths 0.30 m and 0.45 m). During ice sliding, a large portion of the panel is subjected to biaxial tension. Should an initial crack be produced during deformation, continuous torn-open of the outer shell will occur with a steady force (cases with initial dents depths 0.60 m and 0.90 m).

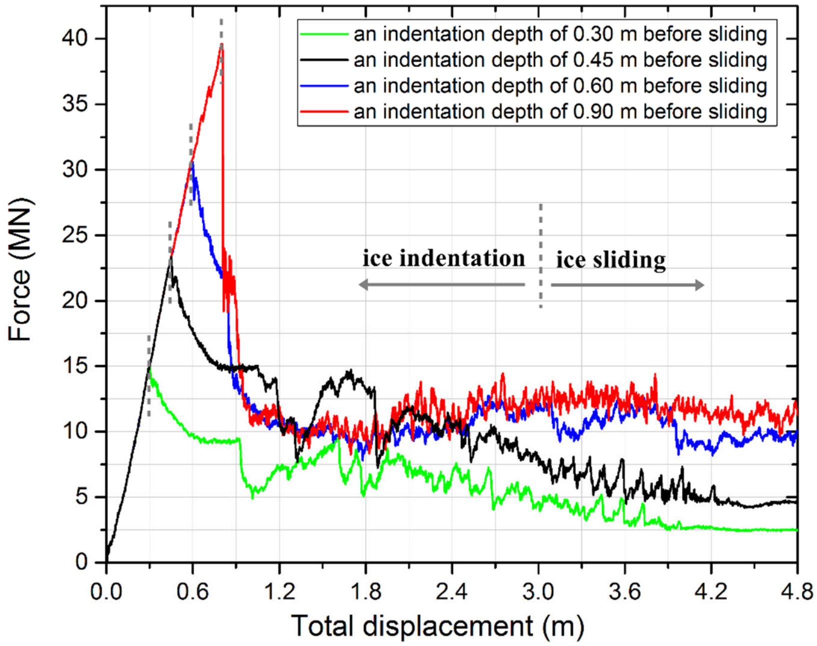

Figure 25. The structural resistance of a semi-submersible column stiffened panel under moving ice loads with different initial dent depths. The total displacement includes both initial indentation stage and subsequent ice sliding stage.

References

AARI 2005. Glaciers at Novaya Zemlya/Sources for Icebergs in the Barents Sea. Research report ordered by Statoil. .

ABRAMOV, V. A. 1996. *Atlas of Arctic Icebergs: The Greenland, Barents, Kara, Laptev, East-Siberian and Chukchi Seas and the Arctic Basin*, Backbone Publishing Company.

ALSOS, H. S. & AMDAHL, J. 2009. On the resistance to penetration of stiffened plates, Part I–Experiments. *International Journal of Impact Engineering,* 36**,** 799-807.

DEZECOT, C. & EIK, K. J. 2015. Barents Sea East Blocks Metocean Design Basis "Fysisk miljø i Barentshavet sørøst,".

DNV-RP-C204 2019. Design against accidental loads. *DNV, DET NORSKE VERITAS*.

DNV-RP-C208 2016. Determination of Structural Capacity by Non-linear FE analysis Methods. *Det Norske Veritas*.

DOWDESWELL, J., BENHAM, T., STROZZI, T. & HAGEN, J. 2008. Iceberg calving flux and mass balance of the Austfonna ice cap on Nordaustlandet, Svalbard. *Journal of Geophysical Research: Earth Surface,* 113.

EIK, K. 2009. Iceberg drift modelling and validation of applied metocean hindcast data. *Cold Regions Science and Technology,* 57**,** 67-90.

FALTINSEN, O. M. 1993. *Sea loads on ships and offshore structures*, Cambridge Univ Pr.

FYLLING, I. On the Statistics of Impact Velocities and Hit Positions Related to Collisions and Mating Operations for Offshore Structures. BOSS, 1994. 297-306.

GEOTECH 1985. Medium Scale Iceberg Impact Simulation Test Program.

HAGEN, J. O., KOHLER, J., MELVOLD, K. & WINTHER, J. G. 2003. Glaciers in Svalbard: mass balance, runoff and freshwater flux. *Polar Research,* 22**,** 145-159.

HANSEN, E., BORGE, J., ARNTSEN, M., OLSSON, A. & THOMSON, M. 2019. Estimating icebergs hazards in the Barents Sea using a numerical iceberg drift and deterioration model. *Proceedings of the 25th International Conference on Port and Ocean Engineering under Arctic Conditions.* Delft.

HONG, L. & AMDAHL, J. 2008. Crushing resistance of web girders in ship collision and grounding. *Marine Structures,* 21**,** 374-401.

IACS 2011. Unified Requirements for Polar Ships: I2–Structural requirements for Polar Class ships INTERNATIONAL ASSOCIATION OF CLASSIFICATION SOCIETIES.

ISO19906 2019. Petroleum and natural gas industries - Arctic offshore structures,International Standard, International Standardization organization, Geneva, Switzerland,.

JORDAAN, I., STUCKEY, P., LIFEROV, P. & RALPH, F. Global and local iceberg loads for an arctic floater. OTC Arctic Technology Conference, 2014. Offshore Technology Conference.

KEGHOUCHE, I., COUNILLON, F. & BERTINO, L. 2010. Modeling dynamics and thermodynamics of icebergs in the Barents Sea from 1987 to 2005. *Journal of Geophysical Research: Oceans,* 115.

KUBYSHKIN, N., BUZIN, I., SKUTIN, A. & GLAZOVSKY, A. Determination of the area of generation of big icebergs in the Barents Sea–temperature distribution analysis. The Sixteenth International Offshore and Polar Engineering Conference, 2006. International Society of Offshore and Polar Engineers.

LIU, Z. & AMDAHL, J. 2019. On multi-planar impact mechanics in ship collisions. *Marine Structures,* 63**,** 364-383.

LØSET, S. 1993. Thermal energy conservation in icebergs and tracking by temperature. *Journal of Geophysical Research: Oceans,* 98**,** 10001-10012.

LØSET, S. & CARSTENS, T. 1996. Sea ice and iceberg observations in the western Barents Sea in 1987. *Cold Regions Science and Technology,* 24**,** 323-340.

LØSET, S., SHKHINEK, K., GUDMESTAD, O. & HØYLAND, K. 2006. *Actions from Ice on Arctic Offshore and Coastal Structures,* Krasnodar, St Petersburg, Russia.

LU, W. & AMDAHL, J. 2019. Glacial Ice and Offshore Structure Impacts under Wave and Current Excitation. *the 25th International Conference on Port and Ocean Engineering under Arctic Conditions (POAC 2019)*.

LU, W., YU, Z., MARNIX, V. D. B., DENNIS, M., RAED, L., VEGARD, H., AMDAHL, J., LØSET, S. & KIM, E. 2019. Loads, Design and Operations of Floaters in the Arctic (Nord ST20). *PTIL - LASTER, DESIGN OG OPERASJON AV FLYTERE I NORDOMRÅDENE (NORD ST20) 2019/313*.

LU, W., YU, Z., VAN DEN BERG, M., LUBBAD, R., AMDAHL, J., LØSET, S. & KIM, E. 2018. Assessment of Structural Damage due to Glacial Ice Impact. *In:* PETROLEUMSTILSYNET (ed.) *PTIL-Konstruksjonssikkerhet i Nordområdene.* Stavanger: Petroleumstilsynet.

MARTIN, T. & ADCROFT, A. 2010. Parameterizing the fresh-water flux from land ice to ocean with interactive icebergs in a coupled climate model. *Ocean Modelling,* 34**,** 111-124.

NORSOK-N003 2007. Action and action effects.

POPOV, Y. N., FADDEEV, O., KHEISIN, D. & YAKOVLEV, A. 1967. Strength of ships sailing in ice. U.S. Army Foreign Science and Technology Center (Translation). .

SANDERSON, T. J. O. 1988. Ice mechanics and risks to offshore structures.

SIMONSEN, B. C. & TÖRNQVIST, R. 2004. Experimental and numerical modelling of ductile crack propagation in large-scale shell structures. *Marine Structures,* 17**,** 1-27.

SPRING, W. 1994. Ice Data Acquisition – Summary Report. Mobil Research Dev. Corp., Dallas E&P Eng., 90 p.

SPRING, W., VINJE, T. & JENSEN, H. Iceberg and sea ice data obtained in the annual expeditions of the Barents Sea Ice Data Acquisition Program (IDAP). Proceedings of 12th International Conference on Port and Ocean Engineering under Arctic Conditions, 1993. 17-20.

STORHEIM, M., ALSOS, H. S. & AMDAHL, J. Evaluation of Nonlinear Material Behavior for Offshore Structures Subjected to Accidental Actions. ASME 2017 36th International Conference on Ocean, Offshore and Arctic Engineering, 2017. American Society of Mechanical Engineers, V03AT02A006-V03AT02A006.

UNIS 2009. Lance Cruise Report in the Barents Sea - May 2009, 57 p.

WAGNER, T. J., STERN, A. A., DELL, R. W. & EISENMAN, I. 2017. On the representation of capsizing in iceberg models. *Ocean Modelling,* 117**,** 88-96.

YU, Z., AMDAHL, J. & SHA, Y. 2018. Large inelastic deformation resistance of stiffened panels subjected to lateral loading. *Marine Structures,* 59**,** 342-367.

YU, Z., LU, W., VAN DEN BERG, M., AMDAHL, J. & LØSET, S. 2019. Glacial ice impacts on an offshore semi-submersible platform, Part 2: damage assessment and ice structure interactions in Accidental Limit States (ALS). *Submitted to journal*.